

AD\_\_\_\_\_

Award Number: W81XWH-04-1-0578

TITLE: Development of Nanomechanical Sensors for Breast Cancer Biomarkers

PRINCIPAL INVESTIGATOR: Shyamsunder Erramilli, Ph.D.

CONTRACTING ORGANIZATION: Boston University  
Boston, MA 02215-1301

REPORT DATE: June 2008

TYPE OF REPORT: Final

PREPARED FOR: U.S. Army Medical Research and Materiel Command  
Fort Detrick, Maryland 21702-5012

DISTRIBUTION STATEMENT: Approved for Public Release;  
Distribution Unlimited

The views, opinions and/or findings contained in this report are those of the author(s) and should not be construed as an official Department of the Army position, policy or decision unless so designated by other documentation.

REPORT DOCUMENTATION PAGE				Form Approved OMB No. 0704-0188	
Public reporting burden for this collection of information is estimated to average 1 hour per response, including the time for reviewing instructions, searching existing data sources, gathering and maintaining the data needed, and completing and reviewing this collection of information. Send comments regarding this burden estimate or any other aspect of this collection of information, including suggestions for reducing this burden to Department of Defense, Washington Headquarters Services, Directorate for Information Operations and Reports (0704-0188), 1215 Jefferson Davis Highway, Suite 1204, Arlington, VA 22202-4302. Respondents should be aware that notwithstanding any other provision of law, no person shall be subject to any penalty for failing to comply with a collection of information if it does not display a currently valid OMB control number. <b>PLEASE DO NOT RETURN YOUR FORM TO THE ABOVE ADDRESS.</b>					
1. REPORT DATE (DD-MM-YYYY) 01-06-2008		2. REPORT TYPE Final		3. DATES COVERED (From - To) 15 May 2004 – 14 May 2008	
4. TITLE AND SUBTITLE  Development of Nanomechanical Sensors for Breast Cancer Biomarkers				5a. CONTRACT NUMBER	
				5b. GRANT NUMBER W81XWH-04-1-0578	
				5c. PROGRAM ELEMENT NUMBER	
6. AUTHOR(S)  Shyamsunder Erramilli, Ph.D.  E-Mail: <a href="mailto:shyam@bu.edu">shyam@bu.edu</a>				5d. PROJECT NUMBER	
				5e. TASK NUMBER	
				5f. WORK UNIT NUMBER	
7. PERFORMING ORGANIZATION NAME(S) AND ADDRESS(ES)  Boston University Boston, MA 02215-1301				8. PERFORMING ORGANIZATION REPORT NUMBER	
9. SPONSORING / MONITORING AGENCY NAME(S) AND ADDRESS(ES) U.S. Army Medical Research and Materiel Command Fort Detrick, Maryland 21702-5012				10. SPONSOR/MONITOR'S ACRONYM(S)	
				11. SPONSOR/MONITOR'S REPORT NUMBER(S)	
12. DISTRIBUTION / AVAILABILITY STATEMENT Approved for Public Release; Distribution Unlimited					
13. SUPPLEMENTARY NOTES					
14. ABSTRACT Nanotechnology has the potential to develop silicon-based arrays for sensing biomarkers associated with breast cancer. In order to develop patient-specific therapy, tailored for each individual, parallel detection of a large number (~103-104) biomarkers may be required. The experience of the semiconductor industry in developing large scale integrated circuits at very low cost can lead to similar breakthroughs in array sensors for biomolecules of interest to the breast cancer community. Nanotechnology can meet the need for high throughput, sensitive methods for rapidly recording biomarker profiles of tumors in individual patients. We report results on the development of arrays of conductance sensors of bio-functionalized silicon nanowires. The fractional change is greatest for the smallest sensors, due to the increased surface-to-volume ratio. The fabrication of arrays of conductance based sensors has now been done, and the nanosensors have been characterized using model systems. This work sets the path for translation of the fabricated sensors to breast cancer clinical practice.					
15. SUBJECT TERMS Nanosensors; Nanotechnology; Breast Cancer; Biomarkers					
16. SECURITY CLASSIFICATION OF:			17. LIMITATION OF ABSTRACT	18. NUMBER OF PAGES	19a. NAME OF RESPONSIBLE PERSON
a. REPORT	b. ABSTRACT	c. THIS PAGE			USAMRMC
U	U	U	UU	22	19b. TELEPHONE NUMBER (include area code)

**Table of Contents**

**Introduction..... 3**

**BODY..... 4**

**Key Research Accomplishments..... 4**

**Reportable Outcomes..... 5**

**Conclusions..... 8**

**References..... 9**

**Appendices.....**

## INTRODUCTION

This is the final report that describes the results of a research effort into the development of nanosensors for breast cancer biomarkers.

### THE PROPOSAL HAD THREE SPECIFIC AIMS:

1. Design of a cantilever based sensor for biomolecular recognition, using Finite-Element simulation.
2. Fabrication of Biofunctionalized Nanoscale Sensors capable of detecting targeted molecules at a concentration of less than 1 ng/ml
3. Characterization of Functionalized nanosensors for selected breast cancer markers, and comparing with existing immunohistochemical and Fluorescence *in situ* hybridization (FISH) techniques on well established biomarkers such as Her-2/*neu*, estrogen and progesterone hormone receptors in tumor tissue, and selected mucin antigens in blood.

We report that we have achieved in full two of the specific aims, and have accomplished part of Aim 3. We have characterized the functionalized nanosensors and have detected the breast cancer biomarker CA15.3 in solution at clinically relevant concentrations. We were not able to perform studies on serum samples from breast cancer patients for the reasons mentioned in the report below. Among the accomplishments of this project, we have discovered an exciting gating principle using electrical methods that has the potential for significantly enhancing the sensitivity to biomarkers and control of the nanoscale structures. We have published this in several papers (References 1-4), and filed a patent application (Ref 5). A startup company, Ninth-Sense Inc, is negotiating to license this idea from our University with the goal of raising fund to expand studies, specifically for breast cancer. We are pleased to report that this DOD funded project has resulted in both research papers, and intellectual property with the potential to benefit breast cancer research and development.

### Key Research Accomplishments

We list here the accomplishments:

Task 1: We have completed simulations to characterize and develop nanoscale cantilever sensors. Simulations conducted in the presence of water show that hydrodynamic effects have to be taken into account in order to properly characterize the sensitivity of these sensors. At the same time, we have performed electrical conductance measurements on nanowire channels in order to assess the sensitivity. A new description for the electrical response of the nanochannels, based on a modified Field-Effect Transistor model, that explains the gating principle and the regime of operation of the sensors that is optimized for biosensing for breast cancer biomarkers.

Task 2: We have successfully used electron beam lithography to fabricate nanosensors and have functionalized them using silanization protocols. Some of the nanomechanical structures our collaboration has developed are among the smallest and highest frequency nanomechanical resonator ever constructed. In performing conductance measurements on the structures, we have discovered a very interesting gating effect that can be used to enhance the sensitivity of the nanosensors.

Task 3: We have successfully shown that the nanosensors respond with sensitivity and specificity to the breast cancer biomarker CA15.3, at clinically relevant concentrations. A new, more sensitive operating regime for the semiconductor sensors has been discovered. This work has led to numerous publications, and a patent application has been filed. A start-up company is negotiating for the license to commercialize this research for breast cancer studies.

## Reportable Outcomes

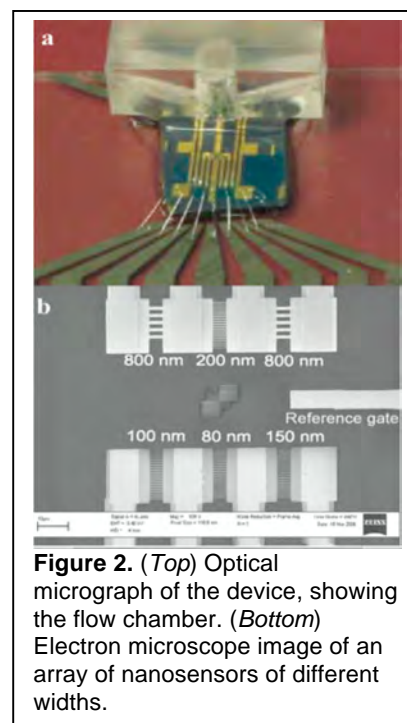
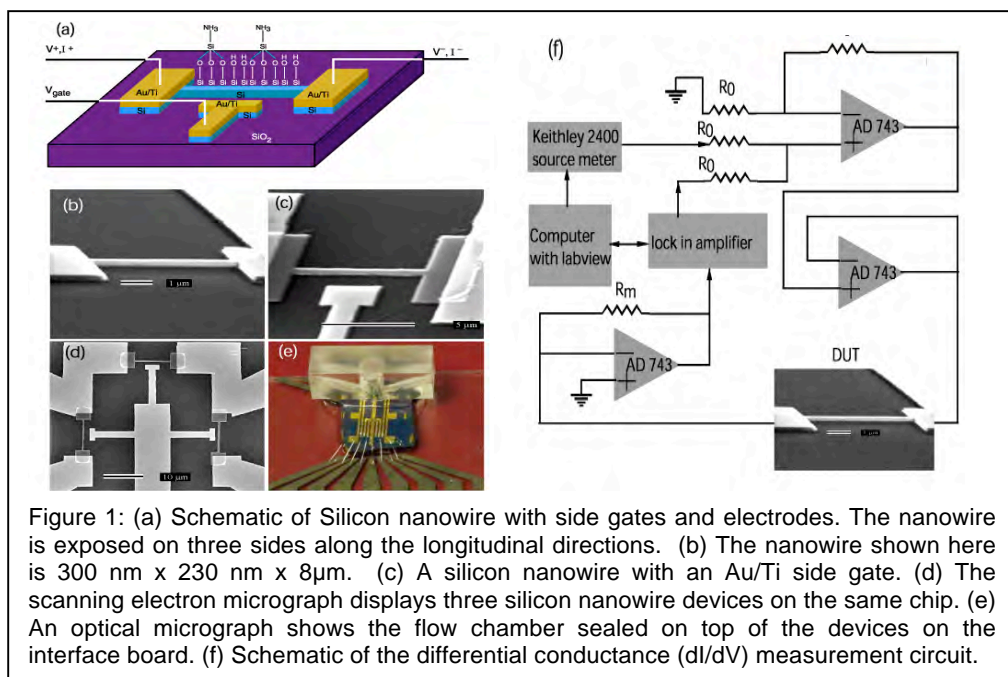
We have used simulations to characterize and develop several types of nanosensors. Figure 1 (a) shows a schematic of the nanochannel sensor developed in this research project. Figure 1 (b-d) show electron microscope images of a single silicon nanowire with contacts on either end, and more complex devices with fabricated side gates for amplification and control. Note that the width of the sensors is 100 nm. The nanowire conductance is modulated as selected biomarker targets bind to the surface of the nanowire. The steps involved include electron-beam lithography, development of the exposed pattern, metallization followed by liftoff, reactive ion etching, and finally metal removal to fabricate the device. These procedures are standard methods of fabrication developed in the semiconductor industry and condensed matter physics, and have the potential to be mass produced. All the steps have been carried out in our laboratory in the Physics department and the Photonics Center at Boston University. The sensitivity of the devices arises from the large surface-to-volume ratio at the nanoscale.

The surface functionalization protocols are based on silane chemistry, and have the ability to bind to any selected antibody for specificity. We have shown that an important new step of Atomic Layer Deposition (ALD) improves the efficiency of silanization. Our research work has shown that both sensitivity and specificity to breast cancer biomarkers has been achieved by silicon nanowire sensors.

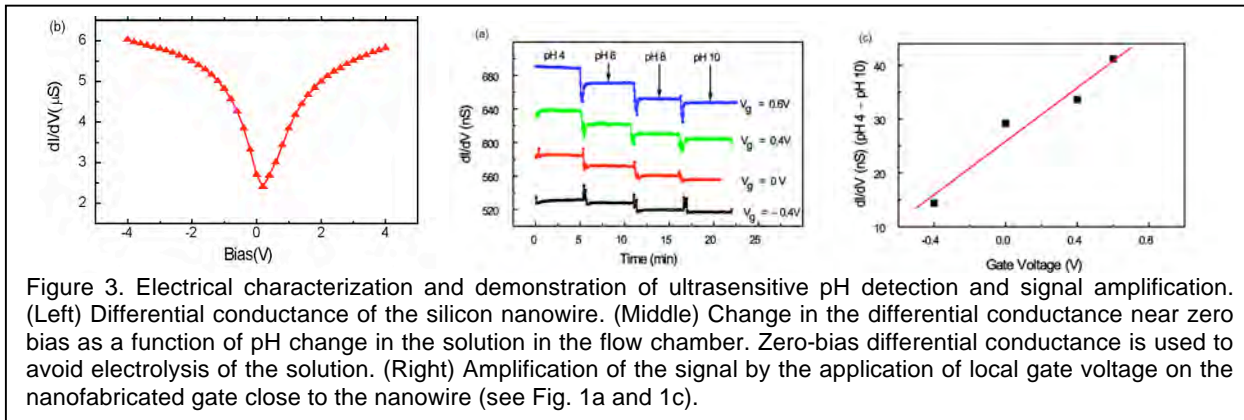
The surface functionalization protocols are based on silane chemistry, and have the ability to bind to any selected antibody for specificity. We have shown that an important new step of Atomic Layer Deposition (ALD) improves the efficiency of silanization. Our research work has shown that both sensitivity and specificity to breast cancer biomarkers has been achieved by silicon nanowire sensors.

Figure 2 shows that we have successfully fabricated an array of nanosensors with controlled dimensions for highly parallel studies on functionalized nanowires. These images demonstrate that lithography methods have the potential for producing special purpose biomarker chips. Unlike fluorescence or optical methods, the chips make measurements purely electrically. The semiconductor industry has long shown that it can make electrical devices smaller, faster and cheaper. In Figure 3(a), an optical micrograph picture also shows the mating to a plastic fluidic channel. The channel has a volume of about 35  $\mu\text{l}$ , and allows for fluid exchange, mixing and sequential testing using a syringe pump. Unlike other microfluidic channel devices, where mixing is a problem, this device allows mixing to occur in the sample volume just above the nanowire. The electrodes connecting to the external electronics are insulated from the serum or buffer. The entire device is mounted onto a semiconductor chip carrier, for easy integration with electronics.

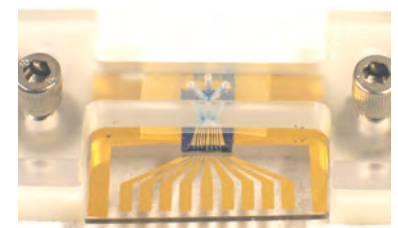
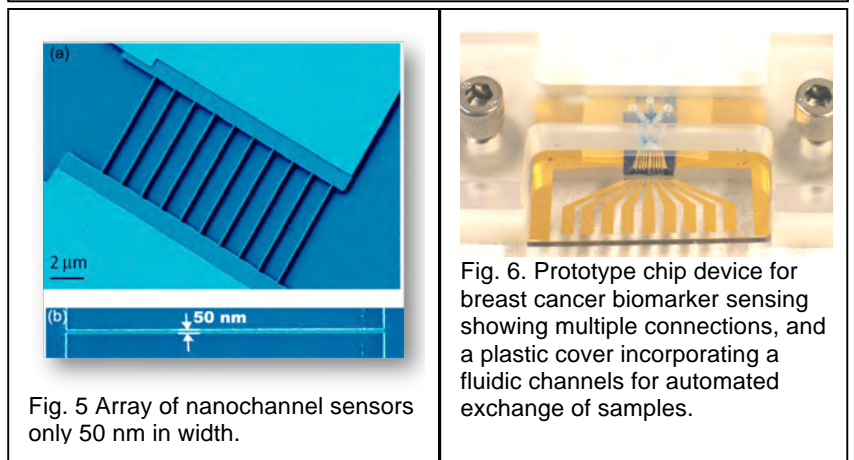
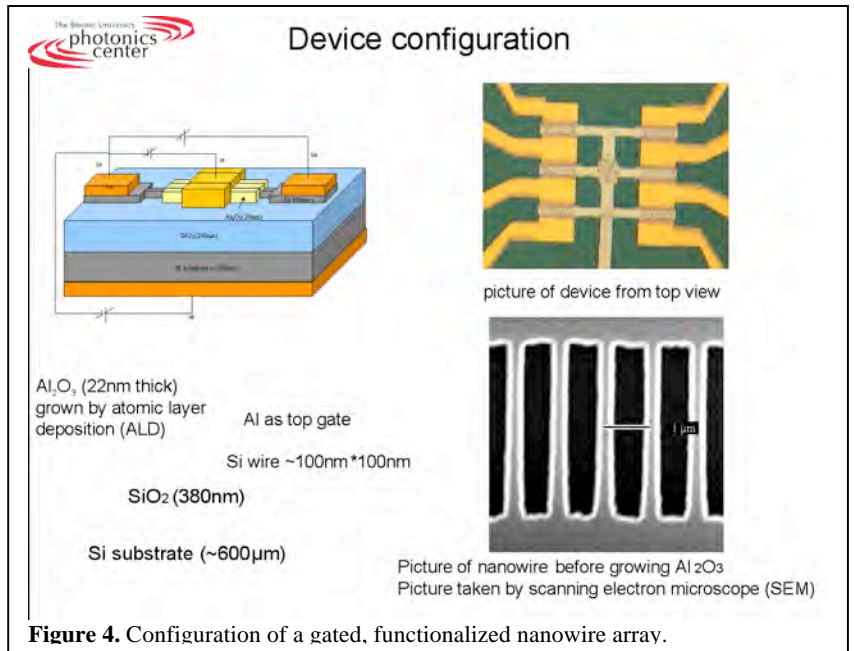
Figure 3 shows the device in operation and the sensitivity to the surface charge density. Electrical characterization of the device showed a novel operating regime of reverse bias. This new operating regime was used to demonstrate sensitivity and signal amplification. The electrical characterization and electron beam



writing was performed in the Physics department, and the rest of the fabrication was carried out at the Photonics Center.



Using these devices, we have been able to study, for the first time, what happens to nanowire conductance as the dimension of the nanowire are systematically varied. Figure 4 shows a parallel set of nanowire channel arrays, used to increase the sensing area for greater sensitivity. The advantage of top-down lithography based methods is evident, in contrast to bottom-up approaches. Other methods that do not use lithography are not able to do this in a systematic way. Our method has complete control of the geometry. Such studies answer the question about ‘why nanotechnology’. We have shown that as the nanowire width is made smaller than about 100 nm, there is dramatic sensitivity to the voltage on the top gate. Binding of the surface markers changes the surface potential and there is also a similar increase in sensitivity to the surface binding. Unexpectedly, we found that there was greater sensitivity in the negative  $V_{ds}$  regime (drain-source voltage). This novel phenomenon is being investigated for its greater potential sensitivity. We found that there is a dramatic increase in the sensitivity to the top gate voltage as the width of the nanowires is decreased below about 100 nm. Figure 5 shows that we have been able to fabricate arrays of 50 nm wide nanochannel wires in a reproducible manner. Finally, Figure 6 shows an assembled nanochannel sample sensor. A plastic cover that incorporates fluidic channels for automated sample exchange using a syringe pump is shown. The device size is about 2 cm in width.





We have now shown the utility of the sensors for detecting a wide range of ionic species and biomarkers. As an example, we have shown that the nanochannel sensors can sense glucose, urea and selected enzyme biomarkers, as described in the publications in the references. The most important experiments involve the testing of the nanowires against a selected biomarker target. We have shown for the first time that silicon nanowires can detect the presence of the cancer antigen, the mucin related antibody CA15.3. We examined the breast cancer serum biomarker protein CA15.3, a product of the *MUC1* gene. Serum levels of CA15.3 reflect tumor burden, and serial assays of CA15.3 can help assess disease progression and treatment response. The upper limit of normal levels of CA15.3 is  $\sim 40$  Units/milliliter (U/ml). We demonstrate the ability of our nanoscale BIOFET device to detect CA15.3 well below this level. Shown in Figure 7a are the measured changes in conductance as the concentration of the CA15.3 is varied, under different bias conditions. Figure 7b shows the differential conductance change induced as the antibody functionalized nanowire is challenged by varying concentrations of CA15.3, along with a measurement using antibiotin as control (Fig. 7b). The data indicate that the conductance change observed is primarily due to specific binding of the biomarker. The inset in Fig. 7a shows the real-time signal when exposed to a calibrated CA15.3 concentration of 36 U/ml. The device response time is less than 60 seconds. The detection limit of CA15.3 concentration is  $\sim 2$  U/ml ( $\sim 10$  pM). Furthermore, the BIOFET response as a function of CA15.3 concentration, demonstrated here over a span of 0 U/ml—2,300 U/ml, underlines the wide dynamic range, which can be applied in a wide range of clinical situations, for both early-stage diagnosis and later-stage prognosis without reconfiguration. Figure 8 shows the level of specificity. The signal response to CA15.3 to a model protein shows the specificity. Some residual non-specific binding does exist, but at a level that can be distinguished easily from background. We have also tested the nanochannel sensors against Prostate Specific Antigen with similar results. However, the small but persistent slope seen with the antibiotin challenge took longer to solve than expected. We have traced the problem to the surface functionalization protocol, which still leaves many surface binding sites to ionic species available. Because of this, even though the response to the desired breast cancer biomarker was clearly greater than that for controls, we postponed studies on clinical specimens. By the time the problem was resolved, by altering our surface functionalization protocol, our funding for the graduate students working on the project had run out and we were not able to recruit patients for studies using our nanosensors. We regard this aspect as a failure on our part. On the positive side, the nanochannel sensors developed here have proven to be of sufficient interest that a start-up company, Ninth-Sense Inc, is negotiating for the license to commercialize the sensors specifically for

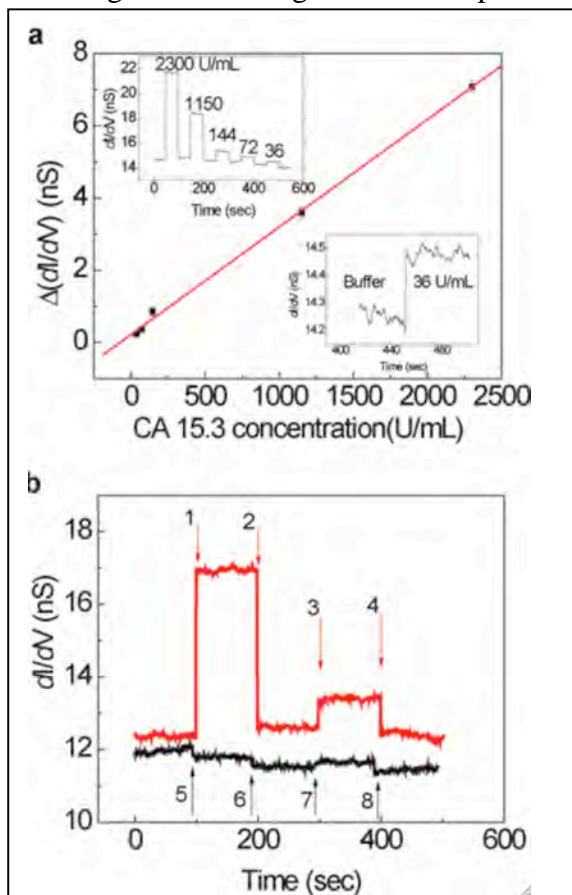


Figure 7. Response of the nanowire to the breast cancer biomarker CA15.3 This is the first demonstration that nanowires can detect the presence of breast cancer biomarkers at clinically

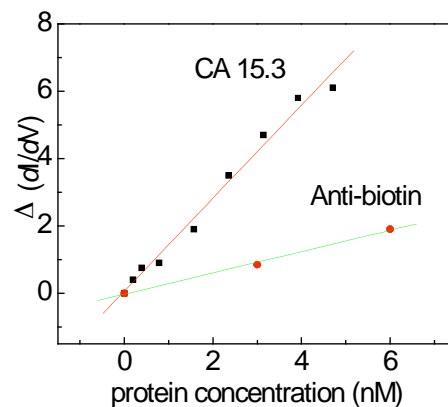


Figure 8. Differential conductance change in the nanowire sensor challenged by CA15.3 and anitbiotin.

breast cancer studies. We are optimistic that the net result of our research will prove to be beneficial to the breast cancer community.

### **Conclusions**

To summarize our key research accomplishments, we have developed new nanosensors and have shown that the silicon nanowires are sensitive to the breast cancer antigen CA15.3. We have discovered a potentially extremely interesting “Gate Control” method for enhancing signal and also for control of the local pH at the femtoliter level. We have also found a novel biasing regime which enhances the sensitivity to a point where the presence of the biomarker at concentrations well below clinical levels can be readily detected. Apart from numerous publications, we hope that the interest shown in the technology by a start-up company will lead to benefits for the breast cancer community.



## References and Publications

1. Y. Chen, X. Wang, S. Erramilli, and P. Mohanty. *Silicon-based nanoelectronic field-effect pH sensor with local gate control*. Applied Physics Letters 89, 223512 (2006).
2. J. Dornnac, A. Kalinowski, S. Erramilli, P. Mohanty "Dynamical Response of Nanomechanical Oscillators in Immiscible Viscous Fluid for in vitro Biomolecular Recognition", *Phys. Rev. Lett.* **96**, 186105 (2006).
3. Yu Chen, Xihua Wang, Mi K. Hong, Shyamsunder Erramilli, Pritiraj Mohanty, and Carol Rosenberg, "Nanoscale field effect transistor for biomolecular signal amplification" *Appl. Phys. Lett.* 91, 243511 (2007).
4. X.Wang, Y. Chen, K. A. Gibney, S. Erramilli, P. Mohanty (2008) "Silicon-based nanochannel glucose sensor", *Appl. Phys. Lett.* **92**, 013903-013905.
5. Y. Chen, X. Wang, M. K. Hong, A. Kalinowski, S. Erramilli, P. Mohanty Patent Pending: (WO 2008/063901)  
NANOCHANNEL-BASED SENSOR SYSTEM FOR USE IN DETECTING CHEMICAL OR BIOLOGICAL SPECIES

# Silicon-based nanoelectronic field-effect pH sensor with local gate control

Yu Chen, Xihua Wang, Shyamsunder Erramilli, and Pritiraj Mohanty<sup>a)</sup>

Department of Physics, Boston University, 590 Commonwealth Avenue, Boston, Massachusetts 02215

Agnieszka Kalinowski

School of Medicine, Carnegie Mellon University and University of Pittsburgh, Pittsburgh, Pennsylvania 15261

(Received 24 August 2006; accepted 6 October 2006; published online 29 November 2006)

The authors demonstrate the operation of a nanoscale field-effect pH sensor engineered from a functionalized silicon nanowire. With this nanofabricated pH sensor, the change in the hydrogen ion concentration or the pH value of a solution can be detected by the corresponding change in the nanowire differential conductance with a resolution of  $\pm 5\text{ nS/pH}$ . Fabrication of selective side gates on the nanowire sensor allows field-effect control of the surface charge on the nanowire by controlling the accumulation of charge carriers with the side-gate voltage. A simple physical model is used to analyze the observed data and to quantify the dependence of the conductance on pH. The development of a nanoscale sensor with physically engineered gates offers the possibility of highly parallel labeling and detection of chemical and biological molecules with selective control of individual array elements. © 2006 American Institute of Physics. [DOI: 10.1063/1.2392828]

Ultrasensitive detection of biological and chemical species is fundamental to the screening and detection of disease, discovery and screening of drugs, as well as gas detection and biomolecular analysis.<sup>1,2</sup> In particular, the ability to detect ions in liquid solutions with ion-selective nanoscale electronic sensors is attractive to a number of fields. For instance, in addition to the detection of proteins, virus, and DNA,<sup>3–6</sup> biocompatible silicon-based sensors have been used for *in vivo* neurological studies such as the detection of calcium and potassium ion concentrations. Furthermore, highly parallel detection by an array of such sensors with control over individual elements offers the possibility of advanced engineering for enhancement in detection sensitivity as well as simultaneous analysis of multiple species.

Nanostructures such as nanowires,<sup>7</sup> nanotubes,<sup>8</sup> nanocrystals,<sup>9</sup> nanocantilevers,<sup>10</sup> and quantum dots<sup>11</sup> are particularly attractive as biosensors, since the critical dimensions of the nanostructures, such as the diameter of the nanowire, are comparable to the sizes of biological and chemical species. The detection sensitivity is therefore greatly enhanced as the signal can be effectively transduced because of large surface-to-volume ratio. In a nanoscale conductor, the surface-to-volume ratio is large because of size, so its electrical property such as conductance is dominated by surface contributions. Therefore, the presence of charged proteins on the surface of an active nanowire induces a large fractional change in the nanowire conductance and enables relatively easy detection.

A silicon nanowire can be used as an ultrasensitive detector by taking advantage of the field effect. A conventional silicon nanowire can be used as a sensor of hydrogen ion concentration or a pH sensor by modifying its surface with 3-aminopropyltriethoxysilane (APTES), which produces amino groups as well as silanol (Si–OH) groups on the nanowire surface. These groups operate as receptors of hydrogen ions, which undergo protonation/deprotonation reactions. In the process, the surface charge on the silicon nanowire

changes, which, in turn, changes the nanowire conductance. In an *n*-type silicon nanowire, with increasing pH, there is an increase in the negative charge on the surface, which acts like a negatively charged gate. This causes the channel of the charge carrier to deplete, therefore the net conductance decreases. The accumulation of carriers by the reception of hydrogen ions can be viewed as a field effect as it modulates the *n*-type field-effect transistor (FET) device.

In a pioneering experiment, Cui *et al.*<sup>7</sup> have demonstrated the operation of a nanoelectronic pH sensor fabricated with a “bottom-up” method. The change in the nanowire conductance as a function of pH was found to be consistent with the previous measurements of pH-dependent surface charge density on silica.<sup>12</sup> The silicon nanowires could be further aligned by a vapor-liquid-solid growth flow technique<sup>13</sup> along the electrodes. Further experiments demonstrated the ability of such sensors to detect biological species such as proteins<sup>3</sup> and virus molecules.<sup>5</sup> Additional control on the conductance of the functionalized FET devices was obtained with the application of a gate voltage to the substrate.

In a fundamentally different approach to device architecture, here we demonstrate the operation of a nanoelectronic pH sensor fabricated with a “top-down” method. The essential advantage of this approach is the complete control over physical and electronic degrees of freedom. The geometry and alignment of the nanowire can be fully controlled by e-beam lithography and standard semiconductor processing techniques. Furthermore, physical gate electrodes next to the nanowire can be fabricated with complete control over their location and size. These local gate electrodes enable controlled accumulation or depletion of surface charge carriers on the nanowire and provide the ability to tune the nanowire conductance necessary for the optimization of the detection sensitivity. In this configuration, the nanowire pH sensor regains the control and the benefits, usual in standard electronic FET devices.

The engineering of our device consists of two fundamental steps: fabrication and functionalization. The silicon nano-

<sup>a)</sup>Electronic mail: mohanty@buphy.bu.edu

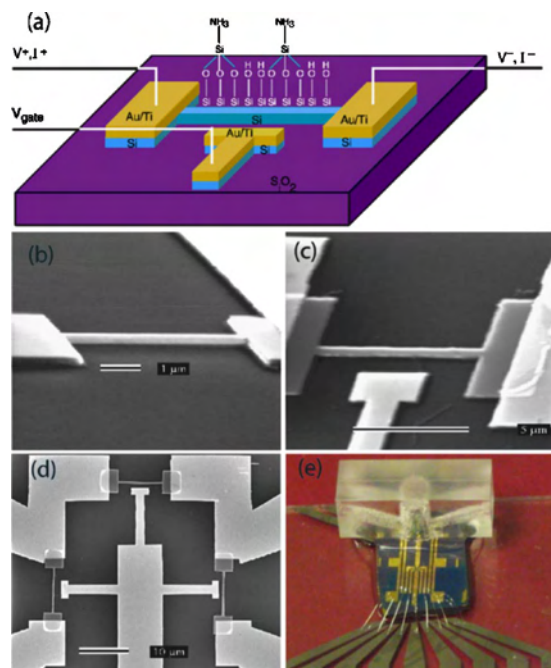


FIG. 1. (Color online) Device schematic diagram, scanning electron micrographs. (a) The schematic diagram of the silicon nanowire with side gates and electrodes. The nanowire is exposed on three sides along the longitudinal direction. (b) The nanowire shown here is 300 nm wide, 230 nm thick, and 8  $\mu\text{m}$  long. (c) A silicon nanowire with a Au/Ti side gate. (d) The scanning electron micrograph displays three silicon nanowire devices on the same chip. (e) An optical micrograph shows the flow chamber sealed on top of the devices on the interface board.

wires along with the side gates and the electrodes are fabricated by standard electron-beam lithography and surface nanomachining. The starting silicon-on-insulator (SOI) wafer has a device-layer thickness of 230 nm and oxide layer thickness of 370 nm with a starting device-layer volume resistivity of 10–20  $\Omega\text{ cm}$ . The device-layer resistivity can be further controlled by doping the wafer by ion implantation of boron with a concentration of  $1 \times 10^{18}/\text{cm}^3$ . After patterning the nanowires and the electrodes in separate steps with separate masks, the structure is etched out with an anisotropic reactive-ion etch. This process exposes the three surfaces of the silicon nanowire along the longitudinal direction as shown in the schematic diagram in Fig. 1(a). After the fabrication of the silicon nanowire and the gold electrodes and gates, a protective layer of polymethylmethacrylate (PMMA) is spun on the surface and only the silicon nanowire is exposed by a secondary e-beam exposure, while the device floor of oxide remains covered. This process allows exposure of only the silicon nanowire to air/solution. The functionalization of the nanowire surface is done by the application of a 2% APTES solution of methanol for 3 h. After multiple rinsing of the device by methanol, the device is dried by nitrogen gas and baked at 80  $^{\circ}\text{C}$  in an oven for 10 min. Following this APTES functionalization technique, the plastic flow chamber is attached to the device with the application of PMMA and silicone gel [Fig. 1(e)]. The flow chamber is designed to include inlet and outlet tubes, connected to a syringe pump, to allow solution flow over the functionalized nanowire inside the chamber. The volume of the flow chamber is estimated to be  $\sim 35\text{ }\mu\text{l}$ .

Measurement of pH-dependent conductance in presence of solution is carried out in two separate methods. One

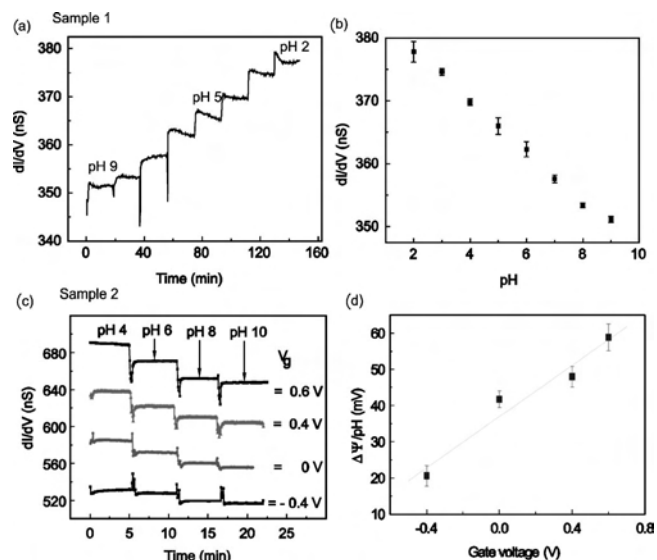


FIG. 2. Zero-bias differential conductance ( $dI/dV$ ) measurements in solution with different pH values. (a)  $dI/dV$  versus time for sample 1, (b)  $dI/dV$  versus pH. (c) Zero-bias differential conductance ( $dI/dV$ ) with increasing pH values of the solution at different gate voltages for sample 2. (d) Effective surface potential change at different gate voltages. The data points for  $V_g = 0.6\text{ V}$  are shifted by 40 nS for clarity in Figs. 2(c). The measurements are done with an ac drive at 37 Hz with an amplitude of 50 mV.

method is the standard two-probe  $I$ - $V$  measurement of the nanowire along with a gate voltage applied to one of the side gates shown in Fig. 1(c). Because of the high resistance of the nanowire, the  $I$ - $V$  characteristic is measured with a Keithley 2400 source meter with a current resolution of 10 pA. Additionally, an Agilent 4339B high-impedance bridge is used for calibration and comparison. In order to discern small changes in the pH-dependent conductance, we have used another more elaborate technique of differential conductance ( $dI/dV$ ) measurement. The measurement circuit includes a small ac modulation (provided by an EG&G 5210 lock-in amplifier), superimposed on the dc bias across the nanowire (provided by the Keithley 2400 source meter). The ac modulation and the dc bias are added by a noninverting summing circuit, which is integrated with the preamplifier circuit. The circuit is then put in a rf-shielded aluminum box to prevent noise pickup. Differential conductance measurements are done by sweeping the dc bias at a constant ac modulation amplitude and measuring the response with the lock-in amplifier, referenced to the ac signal frequency. This approach allows the measurement of zero-bias conductance  $dI/dV|_{V=0}$ , avoiding bias-dependent effects in the solution such as electrolysis.

Figure 2 displays zero-bias differential conductance of the functionalized nanowire in pH solution. The wire is 300 nm wide, 230 nm thick, and 8  $\mu\text{m}$ . Solutions with varying hydrogen ion concentration or pH are made from phosphate buffered saline, containing 10 mM of phosphate and 130 mM of NaCl. The zero-bias conductance of the nanowire increases with increasing pH. Figures 2(a) and 2(b) show an almost linear relation between  $dI/dV$  and pH value of the solution. Further evidence of field effect is demonstrated by zero-bias conductance measurement at different gate voltages, shown in Fig. 2(c). All the measurements are done at room temperature. The zero-bias conductance is tuned by the application of the side-gate voltage. A positive gate bias implies opening of the charge carrier channel, simi-

lar to the inversion layer in silicon devices. A negative gate bias implies depletion or squeezing of the charge carrier channel, similar to depletion layer. The zero-bias conductance increases or decreases depending on positive or negative gate bias, respectively.

Field-effect transistors constitute a rich area of semiconductor physics. The term “FET” covers a large family of devices, which include metal-oxide FET (also called insulated gate field-effect transistor), junction field-effect transistors (JFETs), and so on. It is not clear which model best describes the operation of gated silicon nanowires in solution. The detailed description, as well as the functional dependence of device characteristics on external controls, is different. It is advantageous to describe the operation of the nanowire device in terms of directly measurable experimental quantities of interest.

Our model for interpreting the nanoscale devices in this study is based on a JFET, but with the device characteristics that depend on solution *pH* and ionic strength. Larger scale devices used for ion sensitive measurements are called “ion-selective field-effect transistors” (ISFETs).<sup>14</sup> An explicit comparison with ISFETs may be made by considering the threshold voltage, which determines the current flow in the silicon wire as<sup>14</sup>

$$V_t = V_0 - \Psi, \quad (1)$$

where  $\Psi$  is the effective surface potential which is a function of *pH*, the constant  $V_0$ , and the ionic charge  $q$

$$\Delta\Psi = -2.3\alpha \frac{kT}{q} \Delta pH_{\text{bulk}}. \quad (2)$$

The sensitivity factor  $\alpha$  depends on the geometry and nature of the device and environmental factors such as temperature. It ranges between 0 and 1. Equation (2) suggests that the temperature dependence of the surface potential is complicated. Furthermore, large changes in temperature also strongly influence transport properties of the semiconductor. A detailed study of temperature effects needs to take into account the effect on the concentration and mobility of charge carriers in the semiconductor, the effect of phonons. For ion sensing in aqueous solvents, we restrict our study here to room temperature ( $T=298$  K). Under these conditions, when  $\alpha=1$ ,

$$\frac{\Delta\Psi}{\Delta pH_{\text{bulk}}} = -2.3\alpha \frac{kT}{q} = \sim -60 \text{ mV}. \quad (3)$$

For our device, we consider the conduction channel to be the central region of the nanowire with a depletion region between the channel and the naturally formed  $\text{SiO}_2$  surface. When *pH* of the solution is changed, protonation or deprotonation of the APTES modified surface can change the thickness of the depletion region. So the conductance of the wire changes. This is similar to the operation principle of JFET. However, the wire is in nanoscale. Higher surface-to-volume ratio of the smaller wire can give better sensitivity. Adding different gate voltages shares the same principle of extending or squeezing the conduction channel. So the sensitivity can be improved by adding suitable gate voltage.

In the differential conductance measurement at zero bias, the conductance change due to *pH* is 5 nS/*pH* at  $V_g=0$  V, and the conductance change due to gate voltage is 130 nS/V at *pH*=8. After calibration from these quantities, effective surface potential change  $\Delta\Psi$  is 20 mV/*pH* at  $V_g=-0.4$  V and 60 mV/*pH* at  $V_g=0.6$  V as shown in Fig. 2(d).

Further enhancement of sensitivity of our sensors can be done by reducing the dimensions of the silicon nanowire to increase the effective surface-to-volume ratio, reducing the doping concentration of the starting SOI wafer for optimized conductance, creating a better Ohmic contact between the electrodes and the underlying silicon surface by local doping, and optimizing the flow-chamber design for faster throughput.

In conclusion, we demonstrate fabrication, functionalization, and operation of a nanoelectronic field-effect *pH* sensor. The physically engineered silicon nanowire with side gates is fabricated with standard semiconductor processing techniques. The functionalized silicon nanowire can be controlled with local nanoscale side gates to induce inversion or depletion layers. Our approach offers the possibility of highly parallel detection of ion or charged protein and DNA with local control of individual elements. By selective gating, individual nanowires in an array can be turned on or off during functionalization. Therefore the array can contain multiple receptors for the simultaneous detection of multiple chemical and biological species in a single integrated chip.

The authors acknowledge support by the Department of Defense MSRP program (W81XWH-04-1-0578) and the National Science Foundation (DBI-0242697). One of the authors (X.W.) acknowledges support from a Fellowship at the Center for Photonics, Boston University. The authors thank Rostem Irani, Jiandi Wan, Eric Pennick, and David Osborne for invaluable help and discussion.

<sup>1</sup>M. Ferrari, *Nature (London)* **5**, 161 (2005).

<sup>2</sup>P. Bergveld, *IEEE Trans. Biomed. Eng.* **19**, 342 (1972).

<sup>3</sup>F. Patolsky, G. Zheng, and C. M. Lieber, *Anal. Chem.* **78**, 4260 (2006).

<sup>4</sup>W. U. Wang, C. Chen, K. Lin, Y. Fang, and C. M. Lieber, *Proc. Natl. Acad. Sci. U.S.A.* **102**, 3208 (2005).

<sup>5</sup>Z. Li, B. Rajendran, T. I. Kamins, X. Li, Y. Chen, and R. S. Williams, *Appl. Phys. A: Mater. Sci. Process.* **80**, 1257 (2005).

<sup>6</sup>F. Patolsky, G. Zheng, O. Hayden, M. Lakadamyali, X. Zhuang, and C. M. Lieber, *Proc. Natl. Acad. Sci. U.S.A.* **101**, 14017 (2004).

<sup>7</sup>Y. Cui, Q. Wei, H. Park, and C. M. Lieber, *Science* **293**, 17 (2001).

<sup>8</sup>P. G. Collins, K. Bradley, M. Ishigami, and A. Zettl, *Science* **287**, 1801 (2000); R. J. Chen, S. Bangsaruntip, K. A. Drouvalakis, N. W. S. Kam, M. Shim, Y. Li, W. Kim, P. J. Utz, and H. Dai, *Proc. Natl. Acad. Sci. U.S.A.* **100**, 4984 (2003).

<sup>9</sup>Y. X. Liang, Y. J. Chen, and T. H. Wang, *Appl. Phys. Lett.* **85**, 666 (2004); V. C. Sanz, M. L. Mena, A. Gonzalez-Cortes, P. Yanez-Sedeno, and J. M. Pingarron, *Anal. Chim. Acta* **528**, 1 (2005).

<sup>10</sup>S. R. Manalis, E. B. Cooper, P. F. Indermuhle, P. Keemen, P. Wagner, D. G. Hafeman, S. C. Minne, and C. F. Quate, *Appl. Phys. Lett.* **76**, 1072 (2000); L. Johnson, A. K. Gupta, A. Ghafoor, D. Akin, and R. Bashir, *Sens. Actuators B* **115**, 189 (2006); G. Wu, R. H. Datar, K. M. Hansen, T. Thundat, R. J. Cote, and A. Majumdar, *Nat. Biotechnol.* **19**, 856 (2001).

<sup>11</sup>W. C. W. Chan, and S. Nie, *Science* **281**, 2016 (1998); D. R. Larson, W. R. Zipfel, R. M. Williams, S. W. Clark, M. P. Bruchez, F. W. Wise, and W. W. Webb, *ibid.* **300**, 1434 (2003).

<sup>12</sup>G. H. Bolt, *J. Phys. Chem.* **61**, 1166 (1957).

<sup>13</sup>Y. Huang, X. Duan, Q. Wei, and C. M. Lieber, *Science* **291**, 630 (2001).

<sup>14</sup>P. Bergveld, *Sens. Actuators B* **88**, 1 (2003).



## Dynamical Response of Nanomechanical Oscillators in Immiscible Viscous Fluid for *In Vitro* Biomolecular Recognition

Jerome Dornigac,<sup>1,2</sup> Agnieszka Kalinowski,<sup>3,\*</sup> Shyamsunder Erramilli,<sup>1,3</sup> and Pritiraj Mohanty<sup>1</sup>

<sup>1</sup>Department of Physics, Boston University, 590 Commonwealth Avenue, Boston, Massachusetts 02215, USA

<sup>2</sup>College of Engineering, Boston University, 44 Cummington Street, Boston, Massachusetts 02215, USA

<sup>3</sup>Department of Biomedical Engineering, Boston University, 48 Cummington Street, Boston, Massachusetts 02215, USA

(Received 11 February 2006; published 11 May 2006)

Dynamical response of nanomechanical cantilever structures immersed in a viscous fluid is important to *in vitro* single-molecule force spectroscopy, biomolecular recognition of disease-specific proteins, and the study of microscopic protein dynamics. Here we study the stochastic response of biofunctionalized nanomechanical cantilever beams in a viscous fluid. Using the fluctuation-dissipation theorem we derive an exact expression for the spectral density of displacement and a linear approximation for resonance frequency shift. We find that in a viscous solution the frequency shift of the nanoscale cantilever is determined by surface stress generated by biomolecular interaction with negligible contributions from mass loading due to the biomolecules.

DOI: 10.1103/PhysRevLett.96.186105

PACS numbers: 81.07.-b, 45.10.-b, 82.70.Dd, 83.10.Mj

From single-molecule force spectroscopy [1] to biomolecular recognition of disease-specific proteins such as cancer antigens [2], micron-sized cantilevers have proved to be fundamental to the ultrasensitive detection of small forces. Usually, forces are detected by measuring the deflection of the cantilever. In the dynamic case, shift in the resonance frequency of the cantilever is used to infer the magnitude of force. Micromachining techniques now enable commercial production of such cantilevers with dimensions on the order of 100  $\mu\text{m}$  as well as their routine use in force spectroscopy.

Decreasing the cantilever dimensions to submicron or nanometer scales increases resonance frequency to the megahertz-gigahertz range. The resultant increase in the dynamic range and the measurement speed can provide a better tool for probing single molecules. This could be also used for more sensitive bioimaging techniques and monitoring real-time binding kinetics of ligand-protein binding. For biomolecular recognition in a viscous fluid, force sensitivity can be increased by decreasing the effective viscous damping. Nanoscale cantilevers are hence expected to have dramatically enhanced force sensitivity as smaller cantilevers have lower viscous damping.

In spite of the importance of nanomechanical cantilevers for ultrasensitive *in vitro* force detection, there is no widely accepted description that relates resonance frequency change to concentration or mass loading, over the entire range of viscosity relevant to biomolecular recognition in viscous fluids. In this Letter, starting with a model proposed by Sader [3], we describe the hydrodynamics of a beam, immersed in a viscous fluid, while one of its sides is entirely biofunctionalized. We generalize this model by including an additional term that takes into account the surface stress induced by the layer of mutually interacting biomolecules trapped on the functionalized part of the beam and derive its exact thermal vibrations. We find that, in air, frequency shift of the first nanoscale cantilever

mode is primarily determined by surface stress, while mass-loading effects become relevant for higher order modes. More importantly, in a viscous solution such as water, frequency shift is dominated by surface stress rather than biomolecular mass loading, contrary to conventional expectation.

**Model.**—Neglecting rotatory inertia, shear deformation, and internal damping, the equation of motion for the deflection  $y(x, t)$  of a beam with length  $L$ , width  $b$ , and thickness  $d$ , immersed in a fluid at temperature  $T$  and loaded by a constant axial force  $S$ , is given by [3,4]

$$EI \frac{\partial^4 y}{\partial x^4} - S \frac{\partial^2 y}{\partial x^2} + \mu(x) \frac{\partial^2 y}{\partial t^2} = f_h(x, t) + f_{th}(x, t). \quad (1)$$

$E$  and  $I$  are the Young's modulus and moment of inertia of the (coated) beam, respectively. Thermal vibrations of the beam are induced by the Brownian (Langevin) force per unit length  $f_{th}(x, t)$ . They are small enough for nonlinear convective inertial effects in the fluid to be neglected and for the hydrodynamic loading  $f_h(x, t)$  to be linear in the beam displacement [3]. The linear mass (mass per unit length) of the system  $\mu(x)$  consists of the linear mass of the beam  $\mu_b$ , and the linear mass of the trapped biomolecules  $\mu_l(x)$ . The axial load  $S$  introduced in Eq. (1) describes the mutual interaction of biomolecules adsorbed on the beam [5]. The boundary conditions for Eq. (1) are given by  $y(0, t) = y'(0, t) = 0$ ,  $y''(L, t) = 0$ , and  $EI y'''(L, t) = S y'(L, t)$ , where primes denote spatial derivatives [4].

At higher concentrations, the biomolecules form a uniform layer with linear mass  $\mu_l$  and thickness  $h$  so that

$$\mu(x) = \mu_b + \mu_l = \text{constant}. \quad (2)$$

The mutual interaction of biomolecules within the layer is modeled by taking into account the stress  $\sigma$  they generate on the coated surface of the beam. As shown in Ref. [2], this stress enables the bending of the silicon-nitride microcantilevers with length to thickness ratio  $L/d$ , ranging

from  $10^2$  to  $10^3$ . The resulting static deflection, on the order of a few tenths of microns, is related to surface stress by Stoney's formula [6]. However, for the silicon nanomechanical cantilevers under investigation here ( $L/d \sim 50$ ), Stoney's formula typically yields angstrom-level bendings ( $10^{-5} L$ ). So these nanocantilevers remain almost straight under the influence of surface stress. Nevertheless, as shown in [5], this stress induces an effective axial load,  $S = \sigma L$ , that must be included in Eq. (1). In vacuum, such a model has been studied in Ref. [7].

In addition, biomolecular interaction on the surface results in an effective Young's modulus of the layer  $E_l$  [see Ref. [8]]:

$$EI = E_b I_b + E_l I_l \simeq E_b b d^3 / 12 + E_l h b d^2 / 4. \quad (3)$$

$E_b I_b$  and  $E_l I_l$  are the respective bending rigidities of the beam and the layer (the last equality holds when  $h \ll d$ ). In the opposite limit, biomolecules with mass  $m$  sparsely scattered over the beam at locations  $x_i$  result in

$$\mu(x) = \mu_b + \mu_l(x) = \mu_b + m \sum_i \delta(x - x_i), \quad x_i \in [0, L]. \quad (4)$$

If the average spacing is large compared to their size, their mutual interaction is negligible and  $S = 0$ . Considering that their presence does not substantially affect the moment  $I_b$  of the beam, the bending rigidity of the whole system is the same as for an unloaded beam,  $EI = E_b I_b$ .

*Equations of Motion.*—To solve Eq. (1), we expand the deflection  $y(x, t)$  and the force densities  $f_h(x, t)$  and  $f_{th}(x, t)$  in terms of the modes of the *bare* beam, defined as the beam without the added mass [ $\mu_l(x) = 0$ ] though it includes the tension  $S = \sigma L$ :

$$y(x, t) = \sum_{n=1}^{\infty} y_n(t) \phi_n(\xi), \quad \xi = x/L. \quad (5)$$

Similar expressions hold for the force densities. The eigenmodes  $\phi_n(\xi)$  satisfy the following conditions:

$$\begin{aligned} \phi_n''''(\xi) - \alpha \phi_n''(\xi) &= \beta_n^4 \phi_n(\xi); & \alpha &= \sigma L^3 / EI; \\ \phi_n(0) = \phi_n'(0) &= \phi_n''(1) = 0, & \phi_n'''(1) &= \alpha \phi_n'(1). \end{aligned} \quad (6)$$

The self-adjointness of Eq. (6) makes the modes orthonormal:  $\int_0^1 \phi_n(\xi) \phi_l(\xi) d\xi = \delta_{n,l}$ . From Eq. (6), the eigenvalues  $\beta_n$  are the successive positive roots of

$$1 + (1 + \varepsilon_n^2) \cosh \lambda_n^+ \cos \lambda_n^- + \varepsilon_n \sinh \lambda_n^+ \sin \lambda_n^- = 0, \quad (7)$$

where  $\varepsilon_n = \alpha / (2\beta_n^2)$  and  $\lambda_n^\pm = \beta_n [\sqrt{1 + \varepsilon_n^2} \pm \varepsilon_n]^{1/2}$ . Note that, for  $\varepsilon_n = \alpha / (2\beta_n^2) \ll 1$ , Eq. (7) reduces to the usual clamped-free equation,  $1 + \cos \beta_n \cosh \beta_n = 0$ . As  $\beta_n \propto n$  for large  $n$ , eigenvalues for which  $n \gg \sqrt{\alpha}$  are essentially independent of the surface stress.

Let  $\mu(x) = \mu_b + \mu_l(x)$ . Using Eq. (5), Eq. (1) reduces to

$$M \ddot{y}_n(t) + k_n y_n(t) + \sum_{j=1}^{\infty} \Phi_{nj} \ddot{y}_j(t) = F_{n,h}(t) + F_{n,th}(t). \quad (8)$$

$M = \mu_b L$  is the mass of the beam and  $F_{n,h(th)}(t) = L f_{n,h(th)}(t)$ . The effective stiffness of mode  $n$  is

$$k_n = EI \beta_n^4 / L^3. \quad (9)$$

The real and symmetric matrix has components

$$\Phi_{nj} = L \int_0^1 \mu_l(\xi' L) \phi_n(\xi') \phi_j(\xi') d\xi'. \quad (10)$$

If  $\mu_l(x) = \mu_l$ , then  $\Phi = M_l \mathbf{1}$ , where  $\mathbf{1}$  is the identity matrix and  $M_l = L \mu_l$  is the layer mass. Equation (8) decouples and the mass of modes  $y_n$  becomes the total mass of the system,  $M + M_l$ . But nonuniform mass distributions as in Eq. (4) couple the bare modes of the beam.

Taking the Fourier transform of Eq. (8) and using the expression for the hydrodynamic force [9],

$$\hat{F}_{n,h}(\omega) = M_f \omega^2 \Gamma(\omega) \hat{y}_n(\omega), \quad (11)$$

where  $M_f = \frac{\pi}{4} L \rho_f b^2$  is the mass of the fluid loading the beam and  $\Gamma(\omega) = \Gamma_r(\omega) + i \Gamma_i(\omega)$  is a complex “hydrodynamic function” discussed in detail in [3], we obtain

$$\Lambda(\omega) |\hat{y}(\omega)\rangle = |\hat{F}_{th}(\omega)\rangle. \quad (12)$$

Kets  $|v\rangle$  are column vectors with components  $v_i$ ,  $i \in \mathbb{N}$ . The *non-Hermitian* matrix  $\Lambda(\omega)$  is given by

$$\Lambda(\omega) = \Lambda_0(\omega) - \omega^2 \tilde{\Phi}, \quad (13)$$

where

$$\begin{aligned} \Lambda_0(\omega)_{nj} &= \{k_n - \omega^2 [M_f \Gamma(\omega) + M_n]\} \delta_{nj} \\ \tilde{\Phi}_{nj} &= \Phi_{nj} (1 - \delta_{nj}); & M_n &= M + \Phi_{nn}. \end{aligned}$$

*Spectral densities.*—As the *dissipative* (imaginary) part of the hydrodynamic function is frequency dependent, we apply the generalized fluctuation-dissipation theorem [10] to derive the power spectrum matrix of the stochastic forces  $F_{n,th}$ ,  $S_{\hat{F}}(\omega) = |\hat{F}_{th}(\omega)\rangle \langle \hat{F}_{th}(\omega)|^s$  (the overline denotes thermal averaging, the superscript  $s$  refers to the spectral density, and  $\langle \hat{F}_{th} \rangle$  is the Hermitian conjugate of  $|\hat{F}_{th}\rangle$ ):

$$S_{\hat{F}}(\omega) = \frac{kT}{i\omega} [\Lambda^\dagger(\omega) - \Lambda(\omega)] = 2kTM_f \omega \Gamma_i(\omega) \mathbf{1}, \quad (14)$$

where  $k$  is the Boltzmann constant and  $T$  the temperature. In components, this yields

$$\overline{\hat{F}_{n,th}(\omega) \hat{F}_{p,th}^*(\omega')} = 2kTM_f \omega \Gamma_i(\omega) \delta_{np} \delta(\omega - \omega'). \quad (15)$$

Notice that this expression does not depend on  $\Phi$ . It is the same as for a bare beam. As seen above, the stochastic forces acting on distinct modes are uncorrelated. Nevertheless, their power spectrum is not constant, contrary to the assumption made in Ref. [3], for the frequency dependence of the dissipative part of the hydrodynamic function makes them non-Markovian. Equation (15) is the generalization of the expression derived by Paul and Cross for a single cantilever mode [11]. Now, inverting Eq. (12),



we obtain

$$|\hat{y}(\omega)\rangle = \chi(\omega)|\hat{F}_{th}(\omega)\rangle, \quad \chi(\omega) = \Lambda^{-1}(\omega) \quad (16)$$

and  $|\hat{y}(\omega)\rangle\langle\hat{y}(\omega)| = \chi(\omega)|\hat{F}_{th}(\omega)\rangle\langle\hat{F}_{th}(\omega)|\chi^\dagger(\omega)$ . Spectral averaging the latter and using Eq. (14), we find the power spectrum matrix of the deflection modes

$$S_{\hat{y}}(\omega) = 2kTM_f\omega\Gamma_i(\omega)\chi(\omega)\chi^\dagger(\omega). \quad (17)$$

Introducing  $|\phi_\xi\rangle$  with components  $\phi_n(\xi)$ , the Fourier transform of the deflection (5) reads  $\hat{y}(x, \omega) = \langle\phi_\xi|\hat{y}(\omega)\rangle$  and using Eq. (17), we find its spectral density to be

$$|\overline{\hat{y}(x, \omega)}|^{2^*} = 2kTM_f\omega\Gamma_i(\omega) \left[ \sum_{n=1}^{\infty} \frac{\phi_n^2(\xi)}{M_n^2|A_n|^2} + 2\omega^2 \sum_{n=1}^{\infty} \sum_{p=1}^{\infty} \frac{\phi_n(\xi)\phi_p(\xi)\tilde{\Phi}_{np}\Re(A_p)}{M_n^2M_p|A_n|^2|A_p|^2} + \mathcal{O}(\tilde{\Phi}^2) \right]. \quad (20)$$

In this expression,  $\xi = x/L$ ,  $\tilde{\Phi}_{np}$  is given by Eq. (14), and the quantity  $A_n = \Lambda_0(\omega)_{nn}/M_n$  reads

$$A_n = \omega_n^2 - \omega^2[1 + \lambda_n\Gamma(\omega)], \quad (21)$$

where  $\omega_n = \sqrt{k_n/M_n}$  is the frequency in vacuum,  $\lambda_n = M_f/M_n$ , and  $\Re(A_n)$  is the real part of  $A_n$ . An expression similar to Eq. (20) can be derived for the slope of the deflection provided  $\phi_j(\xi)$  is replaced by  $\phi'_j(\xi)$  and the overall prefactor is divided by  $L^2$ .

Expression (20) is valid for any mass distribution  $\mu_l(x)$  along the beam. For a uniform layer with linear mass  $\mu_l$ ,  $\Phi_{np} = L\mu_l\delta_{np}$ , and then  $\tilde{\Phi}_{np} = 0$ . All modes have the same effective mass,  $M_n = M + L\mu_l$ , and are decoupled. Reinstating in Eq. (20), the second term vanishes and we obtain the *exact* spectral density of a composite beam consisting of the original beam plus the layer. For molecules trapped on the beam at positions  $\xi_i$ , the mass profile given in Eq. (4) leads to  $\Phi_{np} = m\sum_i \phi_n(\xi_i)\phi_p(\xi_i)$  and Eq. (20) is valid up to first order in  $m$  provided the frequency satisfies  $M_f\Gamma_i(\omega) \gg 4M_l$ . Interestingly, if we assume  $N$  molecules to be randomly scattered along the beam in a uniform way and average  $\Phi_{np}$  accordingly, we find  $\langle\langle\Phi_{np}\rangle\rangle = m\sum_i \int \phi_n(\xi_i)\phi_p(\xi_i)d\xi_i = Nm\delta_{np}$ . As the total mass of the trapped molecules is small compared to the mass of the beam, in the first approximation, the average spectral density is the same as the spectral density of their average mass distribution—i.e., the spectral density of a uniform layer of mass  $Nm$ .

In Fig. 1, we compare the bare beam ( $\Phi = 0$ ) spectral density of the deflection slope at the tip of a rectangular silicon nanocantilever ( $E = 160$  GPa,  $\rho = 2.33 \times 10^3$  kg/m<sup>3</sup>) to Sader's result [3] in air and water. The beam dimensions are  $d \times b \times L = 0.2 \times 0.2 \times 10$   $\mu$ m. From [13], at  $T = 27$  °C, the viscosities are  $\eta_{air} = 1.86 \times 10^{-5}$ ,  $\eta_{water} = 8.59 \times 10^{-4}$  kg/(m.s) and the densities are  $\rho_{air} = 1.18$ ,  $\rho_{water} = 997$  kg/m<sup>3</sup>. Typical values for the Reynolds number defined as [3]  $Re = \rho_f b^2 \omega / 4\eta$  are  $Re_{air} \simeq 0.01$  and  $Re_{water} \simeq 0.036$  at resonance. Although different, Sader's formula can be shown to reduce to (20) provided  $\lambda|\Gamma(\omega)| \ll 1$ . This explains why the results are

$$|\overline{\hat{y}(x, \omega)}|^{2^*} = 2kTM_f\omega\Gamma_i(\omega)\langle\phi_\xi|\chi(\omega)\chi^\dagger(\omega)|\phi_\xi\rangle. \quad (18)$$

The total mass of the particles trapped on the beam  $M_l$  is small compared to the mass of the beam. This justifies treating  $\omega^2\tilde{\Phi}$  perturbatively provided its elements stay small compared to the diagonal elements of  $\Lambda_0(\omega)$ . This is indeed the case [12] provided  $M_f\Gamma_i(\omega) \gg 4M_l$ . By inverting Eq. (13), we obtain in first order in  $\tilde{\Phi}$

$$\chi\chi^\dagger = \chi_0\chi_0^\dagger + \omega^2\chi_0(\tilde{\Phi}\chi_0 + \chi_0^\dagger\tilde{\Phi})\chi_0^\dagger + \mathcal{O}(\tilde{\Phi}^2), \quad (19)$$

where  $\chi_0 = \Lambda_0^{-1}$ . Reinstating in Eq. (18), we finally get

very similar in air [ $\lambda|\Gamma(\omega)| \simeq 0.06$  at resonance] while they start to differ in water [ $\lambda|\Gamma(\omega)| \simeq 25$  at resonance].

*Frequency shift.*—As stated earlier, when trapped molecules form a uniform layer, the *exact* spectral density of the beam deflection is given by

$$|\overline{\hat{y}(x, \omega)}|^{2^*} = \frac{2kTM_f\omega\Gamma_i(\omega)}{(M + M_l)^2} \sum_{n=1}^{\infty} \frac{\phi_n^2(\xi)}{|A_n|^2}, \quad (22)$$

where  $M_l$  is the mass of the layer and where  $A_n$  is given in Eq. (21) with  $M_n = M + M_l$ . When the peaks of Eq. (22) are sharp enough, the hydrodynamic function is almost constant in their vicinity and the resonant frequency satisfies the self-consistent equation:

$$\omega_{R,n}^2 = f(\omega_{R,n}, M_n)k_n, \quad f = \frac{1}{3} \frac{R + \sqrt{4R^2 + 3I^2}}{R^2 + I^2}, \quad (23)$$

where  $R = M_n + M_f\Gamma_r$ ,  $I = M_f\Gamma_i$ , and  $\Gamma_{r,i} \equiv \Gamma_{r,i}(\omega_{R,n})$ . From the expression (23), the mass and stiffness variations due to the layer,  $\delta M$  and  $\delta k_n$ , induce a relative frequency shift between a bare and a loaded beam:

$$\frac{\delta\omega_{R,n}}{\omega_{R,n}} = \frac{1}{2 - \omega_{R,n} \frac{\partial \ln f}{\partial \omega_{R,n}}} \left[ \frac{\delta k_n}{k_n} + \frac{\partial \ln f}{\partial M} \delta M \right]. \quad (24)$$

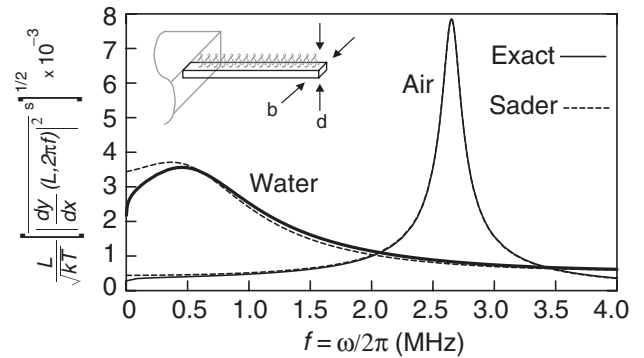


FIG. 1. Inset: schematic diagram of the beam with a layer of molecules on its functionalized side. Main figure: exact spectral density of the deflection slope of a silicon nanobeam without molecular layer. Calculations done in air and water (solid lines) compared to Sader's results [3] (dashed lines).

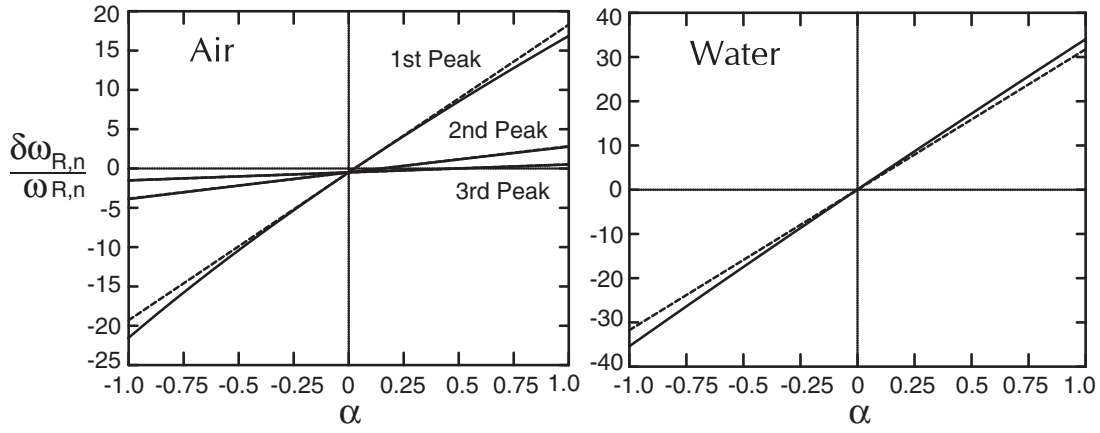


FIG. 2. Relative frequency shift (in %) in air and water vs the dimensionless stress,  $\alpha = \sigma L^3/EI$ .  $M_l = M/100$  and  $E_l = 0$ . Other parameters are the same as in Fig. 1. Solid line: exact result from Eq. (22). Dotted line: linear approximation from Eqs. (24) and (25).

Here,  $\delta M = M_l$  and its prefactor in Eq. (24) takes into account dissipative ( $M_f \Gamma_i$ ) and fluid mass loading ( $M_f \Gamma_r$ ) effects. According to (9), the two contributions to the stiffness  $\delta k_n$  come from the bending rigidity,  $E_b I_b \rightarrow E_b I_b + E_l I_l$ , and from the surface stress through the eigenvalue  $\beta_n(\alpha)$ . From Eqs. (3) and (7), we find

$$\frac{\delta k_n}{k_n} = \frac{3hE_l}{dE_b} + \frac{2T_n t_n + \beta_{0,n}(T_n + t_n)}{\beta_{0,n}^3(t_n - T_n)} \alpha, \quad (25)$$

where  $\beta_{0,n}$  is the  $n$ th root of  $\cosh(\beta) \cos(\beta) + 1 = 0$  and where  $T_n = \tanh \beta_{0,n}$ ,  $t_n = \tan \beta_{0,n}$ . The last term of (25) has been obtained from (7) in perturbation. It is valid when  $\alpha \ll n^2$  and vanishes as  $n \rightarrow \infty$ .

Using the same data as in Fig. 1, we display in Fig. 2 the relative frequency shift in air (left) and water (right) versus the dimensionless surface stress  $\alpha$ . The exact shift is evaluated from the spectral density in Eq. (22) and compared to its linear approximation in Eq. (24). The layer mass has been arbitrarily fixed to 1% of the beam mass and  $E_l$  set to zero, hence the negative offset observed in air at  $\alpha = 0$ . For typical values of the surface stress,  $\sigma \sim 10^{-2} \text{ J m}^{-2}$  [see Wu *et al.* in Ref. [2]],  $|\alpha| \lesssim 1$ . In air,  $\lambda |\Gamma(\omega_{R,n})| \ll 1$ , and  $f \sim 1/M$ . Then,  $\partial \ln f / \partial M \sim -1/M$ ,  $\partial \ln f / \partial \omega_{R,n} \sim 0$ , and we recover the usual frequency shift for a linear oscillator in vacuum. As seen on the left panel, the first peak is the most sensitive to  $\alpha$ . The deviation of the data from the linear result in Eq. (25) indicates that the condition  $\alpha \ll n^2$  with  $n = 1$  becomes violated. This effect disappears for the second and third peaks that are less sensitive to  $\alpha$ . In water (right panel), a single broad peak occurs. Equation (23) loses its accuracy but the frequency shift in Eq. (24) derived from it is still acceptable. The contribution of  $\partial \ln f / \partial M$  becomes negligible while  $\partial \ln f / \partial \omega_{R,n} \sim -\partial \ln \Gamma_i / \partial \omega_{R,n}$  becomes important, hence the increase in the slope of the relative frequency shift versus  $\alpha$  in water compared to air.

In conclusion, we treat the thermal response of biofunctionalized nanocantilevers with a generalized fluctuation-dissipation relation. In a viscous fluid like water, the reso-

nance frequency shift for a continuous distribution of biomolecules on the cantilever surface is found to be dominated by surface stress rather than the mass loading of biomolecules.

We acknowledge support by the Department of Defense MSRP program (W81XWH-04-1-0578) and the National Science Foundation (DBI-0242697).

\*Present address: University of Pittsburgh MSTP, 526 Scaife Hall, 3550 Terrace Street, Pittsburgh, PA 15261.

- [1] M. B. Viani *et al.*, J. Appl. Phys. **86**, 2258 (1999).
- [2] G. Wu *et al.*, Nat. Biotechnol. **19**, 856 (2001); Proc. Natl. Acad. Sci. U.S.A. **98**, 1560 (2001).
- [3] J. E. Sader, J. Appl. Phys. **84**, 64 (1998); C. P. Green and J. E. Sader, J. Appl. Phys. **98**, 114913 (2005).
- [4] J. L. Humar, *Dynamics of Structures* (Prentice-Hall, Englewood Cliffs, NJ, 1990), p. 654.
- [5] G. Y. Chen *et al.*, J. Appl. Phys. **77**, 3618 (1995); P. Müller and R. Kern, Surf. Sci. **301**, 386 (1994).
- [6] G. Stoney, Proc. R. Soc. A **82**, 172 (1909); J. E. Sader, J. Appl. Phys. **89**, 2911 (2001).
- [7] P. Lu *et al.*, Mater. Phys. Mech. **4**, 51 (2001); Q. Ren and Y.-P. Zhao, Microsystem Technologies **10**, 307 (2004).
- [8] J. P. Gere and S. P. Timoshenko, *Mechanics of Materials* (PWS Publishing Company, Boston, 1997).
- [9] L. Rosenhead, *Laminar Boundary Layers* (Clarendon, Oxford, 1963), p. 391; We assume here that the presence of a layer of molecules binding to the beam does not affect the hydrodynamic force.
- [10] N. Smith, J. Appl. Phys. **90**, 5768 (2001); **92**, 3877 (2002).
- [11] M. R. Paul and M. C. Cross, Phys. Rev. Lett. **92**, 235501 (2004).
- [12] As  $\Gamma_i(\omega) \rightarrow 0$  when  $\omega \rightarrow \infty$ ,  $M_f \Gamma_i(\omega) \gg 4M_l$  is violated at some critical frequency beyond which Eq. (19) does not hold. A “nonperturbative” treatment of the inversion of  $\Lambda(\omega)$  is then in order. It can be done approximately by analytically inverting the  $2 \times 2$  or  $3 \times 3$  sub-block of  $\Lambda(\omega)$  surrounding the small diagonal element.
- [13] J. W. M. Chon, P. Mulvaney, and J. E. Sader, J. Appl. Phys. **87**, 3978 (2000).

# Nanoscale field effect transistor for biomolecular signal amplification

Yu Chen, Xihua Wang, Mi K. Hong, Shyamsunder Erramilli, and Pritiraj Mohanty<sup>a)</sup>  
*Physics Department, Boston University, Boston, Massachusetts 02215, USA*

Carol Rosenberg

*Department of Medicine, Boston University School of Medicine, Boston Massachusetts 02118, USA*

(Received 5 October 2007; accepted 18 November 2007; published online 14 December 2007)

We report amplification of biomolecular recognition signal in lithographically defined silicon nanochannel devices. The devices are configured as field effect transistors (FET) in the reversed source-drain bias region. The measurement of the differential conductance of the nanowire channels in the FET allows sensitive detection of changes in the surface potential due to biomolecular binding. Narrower silicon channels demonstrate higher sensitivity to binding due to increased surface-to-volume ratio. The operation of the device in the negative source-drain region demonstrates signal amplification. The equivalence between protein binding and change in the surface potential is described. © 2007 American Institute of Physics. [DOI: 10.1063/1.2822445]

Ultrasensitive recognition of molecules is important in basic science, as well as in pharmacology and medicine for the analysis of biomarkers.<sup>1,2</sup> Nanotechnology has made it possible to enhance detection sensitivity by using nanowires,<sup>3,4</sup> nanotubes,<sup>5</sup> nanocrystals,<sup>6</sup> nanocantilevers,<sup>7,8</sup> and quantum dots.<sup>9</sup> The signal arising from biomolecular binding on the surface can alter measurable physical properties of the nanoscale device such as electrical conductance with increased sensitivity due to the large surface-to-volume ratio.

A silicon nanowire can be used as the source-drain channel of a field effect transistor (FET). In conventional FETs, lithographic methods are used to fabricate gates at the bottom, the top, or the side. In addition, the nanochannel surface can be functionalized with specific receptor or antibody. In a fluid, the ligand (or antigen) can bind to the receptor, which results in a change in the surface charge profile and the surface potential. Essentially, this binding behaves as a field effect. The conductance and the  $I$ - $V$  characteristics of the nanowire can therefore be used to characterize biomolecular binding—for instance, to determine concentration and binding dissociation constant. In this letter, we show that characteristics of differential conductance  $dI/dV$  can be used for even higher sensitivity in the field effect due to biomolecular binding. In particular,  $dI/dV$  characteristics allow measurement at low bias, essential for avoiding electrolysis.

In a series of experiments, Lieber and co-workers have demonstrated the operation of nanowire FET sensors fabricated with a bottom-up method, using chemically grown silicon nanowires. These nanowire field-effect sensors show significant advantages of real-time, label-free and highly sensitive detection of a wide range of analytes, including proteins, nucleic acids, small molecules, and viruses in single-element or multiplexed formats.<sup>10</sup> These bottom-up approaches, however, have limitations arising from the lack of control in materials and fabrication engineering. In contrast, top-down methods of fabrication by  $e$ -beam lithography or submicron optical lithography enable scalable manufacturing.

Here, we demonstrate that the differential conductance  $dI/dV$  characteristics of silicon nanowire field effect transistors with width below 200 nm show strong dependence on gate voltage. We use the peak position of the  $dI/dV$  curve to characterize antibiotic detection with sub-ng/ml sensitivity by functionalizing the silicon nanowire surface with biotin. From this measurement, we can extract the dissociation constant of biotin-antibiotin binding to be  $5.2 \times 10^{-10}$  M, in good agreement with other measurements.

By functionalizing the silicon nanowire surface with biotin, we show that the device can be used to characterize protein binding. Furthermore, we show equivalence between the field effect created by the biomolecular binding and the reference gate voltage. This equivalence allows the characterization of ligand-receptor binding by determining the calibrated gate voltage dependence rather than measuring the more cumbersome concentration dependence.

Our devices are fabricated by standard  $e$ -beam lithography and surface nanomachining. The starting (100) SOI wafer has a device layer thickness of 100 nm and oxide layer thickness of 380 nm, on a 600  $\mu$ m boron-doped substrate. The device-layer volume resistivity ranges from 10–20  $\Omega$  cm. After patterning the nanowires and the electrodes in separate steps, the structure is etched out with an anisotropic reactive-ion etch. This process exposes the three surfaces of the silicon nanowire along the longitudinal direction, resulting in structure with three-dimensional relief and a large surface-to-volume ratio. Finally, a layer of  $\text{Al}_2\text{O}_3$  (5–20 nm thick) is grown by atomic layer deposition. A plastic flow cell is used to bathe the device in a small volume of fluid (20–30  $\mu$ L) avoiding the mixing problem of microfluidic channel.<sup>11</sup>

The device pictures and measurement configurations are shown in Fig. 1. The use of parallel nanowires improves the average signal while maintaining a high surface-to-volume ratio. A fabricated top gate is used to characterize current-voltage relation of the device in Fig. 1(c). Small changes in the conductance of the device are best measured by considering the differential conductance  $g(V_{ds}, V_g) = (\partial I_{ds} / \partial V_{ds})_{V_g}$  with the measurements made at constant top gate voltage  $V_g$ . In biological sensing measurements [Fig. 1(d)], an Ag/AgCl reference gate is used. The conductance is a function of the

<sup>a)</sup>Electronic mail: mohanty@physics.bu.edu.



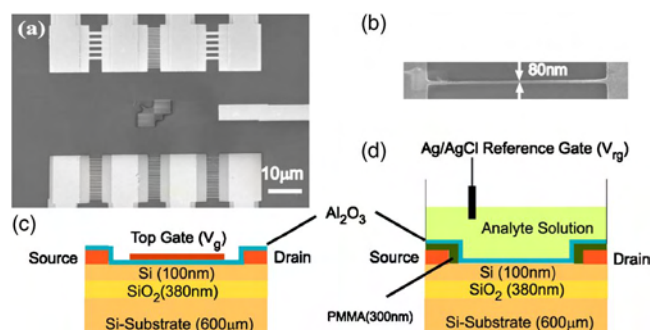


FIG. 1. (Color) Device configuration. Scanning electron micrographs of (a) multiple sensor array and (b) single wire. (c) Schematic of device cross-sectional view with top gate geometry. (d) Schematic of the cross-sectional view of the device, showing reference gate geometry.

bias voltage  $V_{ds}$ , the gate voltage  $V_g$ , or equivalently the surface potential, which can be changed either by changing  $V_{rg}$  or the concentration of charged biomolecules.<sup>12</sup>

Figure 2(a) is the characteristic of the device with a wire width of 350 nm. Figure 2(c) shows the characteristic  $I$ - $V$  curve for a 80 nm device. In Figures 2(b) and 2(d), each curve corresponds to differential conductance measurements at fixed values of  $V_g$ , ranging from  $-1$  to  $+3$  V. At large negative  $V_{ds}$ , all the curves start with a common nonzero value of  $g$ . Such a universal value suggests that conductance is dominated by the Schottky barrier at the junction.<sup>13</sup> Figure 2(b) shows differential conductance for the 350 nm wire as a function of  $V_{ds}$ , which shows a peak in differential conductance near 0 V. As  $V_{ds}$  is increased above a threshold voltage  $V_{th}$ , the slopes of both  $I$ - $V$  characteristic and differential conductance increase. For the 350 nm wire, the differential conductance peak position in Fig. 2(b) is insensitive to  $V_g$ . In contrast, the peak position in Fig. 2(d) is strongly dependent on  $V_g$ . The sensitivity of the conductance peak of the device with narrower width comes from the threshold voltage change. In our model,  $V_{th}$  is linearly dependent on the surface-to-volume ratio

$$\frac{A_{sur}}{V_{vol}} = \frac{(w + 2H)L}{wHL} = \frac{w + 2H}{wH}.$$

Here,  $w$  is the width of the wire,  $H$  is the thickness of the device layer, and  $L$  is the length of the wire. The peak position of the differential conductance at zero top gate voltage is plotted as a function of the nanowire width in Fig. 2(e). Following the methods given in Ref. 14, the conductance peak of the  $dI/dV$  versus  $V_{ds}$  can be calculated in a semiconductor model. With increased surface-to-volume ratio, and hence a higher threshold voltage, the conductance channel is closed at zero bias. A higher gate voltage, i.e., a larger negative bias voltage, is then needed to open the narrow wire channel. Therefore, the conductance peak shifts to negative drain voltage [Fig. 2(e), red points].

In the experiment, the reference gate is immersed in the solution, and a back gate voltage is applied to the substrate. In an array of sensors, the solution reference gate voltage  $V_{rg}$  is common to all the nanowires. However, the source-drain voltage  $V_{ds}$  for each nanowire in the nanosensor array can be controlled individually. In this more flexible configuration, the high voltage required for the back gate can be avoided.<sup>11</sup> At the same time, after channel is opened gradually by  $V_{ds}$ , the sensitivity of the device can be amplified. This naturally implies a region of operation at negative bias for high sensitivity measurements.

The signal amplification effect in reverse bias is demonstrated in protein (antibiotin) measurements. Silicon nanowires, functionalized with biotinylated bovine serum albumin, are used to detect antibiotin in 1 mM NaCl and 1 mM phosphate buffer solution. At the concentration of salt used in solution, the Debye screening length  $\lambda_D$  at room temperature is about 9.6 nm.  $\lambda_D$  is sufficiently large that the surface potential is sensitive to protein binding, but short enough to screen out biomolecules in solution.<sup>11,15</sup> All solutions used in the measurements are dialyzed to maintain constant ionic strength. The differential conductance change  $\Delta g$  due to 100 ng/ml antibiotin in the solution is  $0.02 \pm 0.01$  nS at  $V_{ds}$

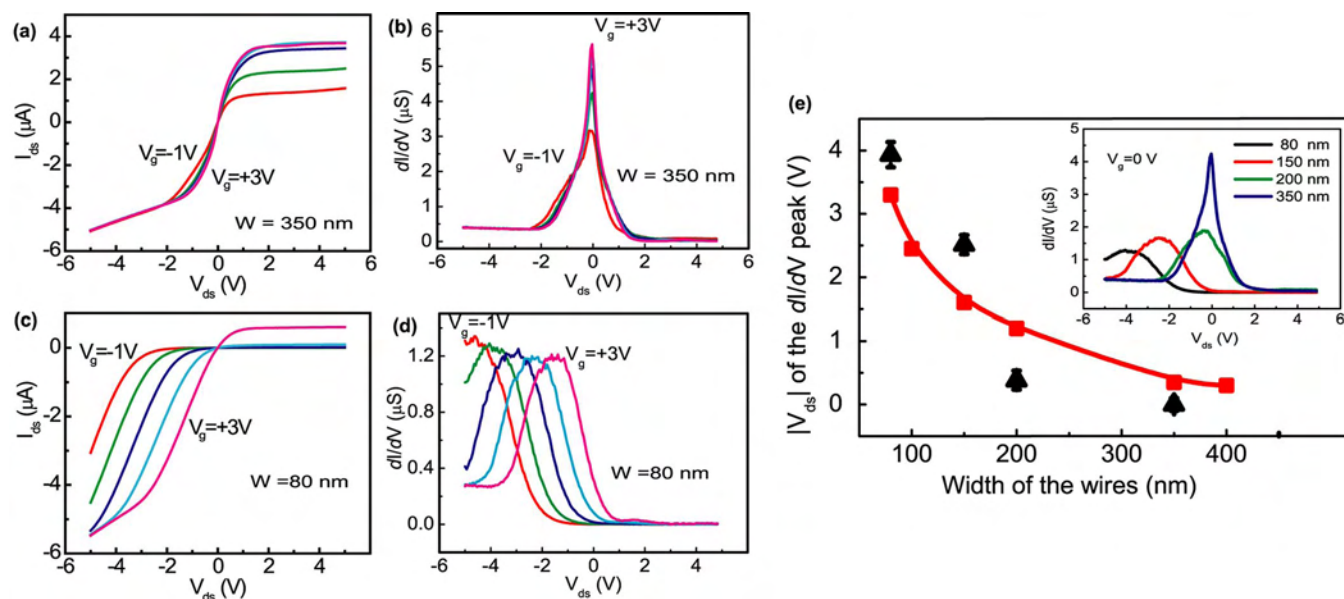


FIG. 2. (Color) Width dependence of the device  $I$ - $V$  characteristics. [(a) and (b)]  $I_{ds}$  and  $dI/dV$  vs source drain voltage  $V_{ds}$  at different top gate voltage  $V_g$  ( $-1$  to  $+3$  V with 1 V step increase) for 350 nm wires. [(c) and (d)]  $I_{ds}$  and  $dI/dV$  vs  $V_{ds}$  at different  $V_g$  ( $-1$  to  $+3$  V with 1 V step increase) for 80 nm wires. (e) Peak position of the  $dI/dV$  peak at  $V_g = 0$  V for devices with different width. Red points show the simulation results used in the model in Ref. 14. The inset is the differential conductance as the function of source drain voltage at  $V_g = 0$  V for different wire widths.

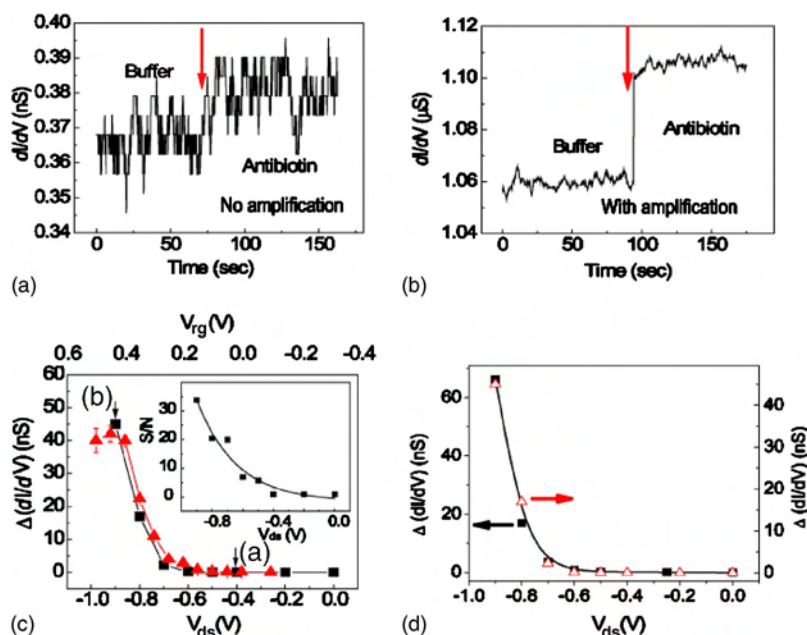


FIG. 3. (Color) [(a) and (b)] Differential conductance vs time. The phosphate buffer is first injected, followed by a 100 ng/mL of antibiotic in the same buffer, with data acquisition being stopped for 30 s following the injection. The bias is set at  $V_{ds} = -0.4$  V and  $V_{ds} = -0.9$  V, respectively. (c) Change in the differential conductance of the device introduced by antibiotic at different  $V_{ds}$  (bottom axis, with fixed  $V_{rg} = 0.3$  V, black solid squares). Red solid triangles are the data at different  $V_{rg}$  (top axis, with  $V_{ds} = 0$  V). Inset is the signal noise ratio of the device at different  $V_{ds}$ . (d) Comparison of conductance change introduced by 5 mV of reference gate voltage change (black dots, left axis) and 100 ng/ml of antibiotic solution (red triangles, right axis).

$= -0.4$  V [see Fig. 3(a)], while  $\Delta g$  is  $45 \pm 0.1$  nS at  $V_{ds} = -0.9$  V [see Fig. 3(b)]. The signal-to-noise ratio increases from 2 to 34 [see Fig. 3(c) inset]. The signal due to 100 ng/ml antibiotic injection is plotted as a function of  $V_{ds}$  and  $V_{rg}$  [see Fig. 3(c)]. This plot clearly shows the effect of reverse bias amplification.

The change  $\Delta g$  above, due to concentration change at fixed reference gate voltage, can be compared to the change caused by varying the reference gate voltage while keeping the concentration fixed. An equivalence between the surface potential change and concentration change is then established.  $\Delta g$  introduced by 100 ng/ml ( $\sim 660$  pM) of antibiotic is equivalent to a gate voltage change of  $7.2 \pm 0.3$  mV [see Fig. 3(d)].

The fundamental advantage of our label-free device architecture is the combination of high detection sensitivity and standard semiconductor-based fabrication techniques, suitable for scalable manufacturing. We operate the device in the reverse bias region without applying high voltage to the back gate<sup>11</sup> or to the reference gate voltage in the solution. Our device configuration allows device-level signal amplification and the required degree of control to enable large-scale parallel architecture for detection of multiple target molecules. This combination is important for any clinical application, including disease screening, diagnosis, monitoring, and prognosis, all of which require fast analysis time, small sample volume, and low cost.

In conclusion, we fabricate silicon nanowire channel FET sensors by a top-down *e*-beam lithography method. Differential conductance characteristics of the devices show dependence on the source-drain channel width of the nanoscale sensor. We take advantage of the strong dependence in the reverse-bias region to demonstrate amplification of biomolecular binding signal by modulating the top gate voltage.

The operation of the device at low reference gate voltage prevents electrolysis. By comparing the signal generated by protein binding with the change in the reference gate voltage, we establish an equivalence between the effect arising due to the concentration-dependent surface charge density and the tunable surface potential in the silicon nanowires.

The authors acknowledge support from the Department of Defense and the National Science Foundation and this work is performed in part at the Photonics Center.

- <sup>1</sup>M. Ferrari, *Nature (London)* **5**, 161 (2005).
- <sup>2</sup>H. G. Craighead, *J. Vac. Sci. Technol. A* **21**, S216 (2003).
- <sup>3</sup>Y. Cui, Q. Wei, H. Park, and C. M. Lieber, *Science* **293**, 1289 (2001).
- <sup>4</sup>Y. Chen, X. Wang, S. Erramilli, P. Mohanty, and A. Kalinowski, *Appl. Phys. Lett.* **89**, 223512 (2006).
- <sup>5</sup>P. G. Collins, K. Bradley, M. Ishigami, and A. Zettl, *Science* **287**, 1801 (2000).
- <sup>6</sup>V. C. Sanz, M. L. Mena, A. Gonzalez-Cortes, P. Yanez-Sedeno, and J. M. Pingarron, *Anal. Chim. Acta* **528**, 1 (2005).
- <sup>7</sup>G. Shekhawat, S.-H. Tark, and V. P. Dravid, *Science* **311**, 1592 (2006).
- <sup>8</sup>J. Dornigac, A. Kalinowski, S. Erramilli, and P. Mohanty, *Phys. Rev. Lett.* **96**, 186105 (2006).
- <sup>9</sup>D. R. Larson, W. R. Zipfel, R. M. Williams, S. W. Clark, M. P. Bruchez, F. W. Wise, and W. W. Webb, *Science* **300**, 1434 (2003).
- <sup>10</sup>G. Zheng, F. Patolsky, Y. Cui, W. U. Wang, and C. M. Lieber, *Nat. Biotechnol.* **23**, 1294 (2005).
- <sup>11</sup>E. Stern, J. F. Klemic, D. A. Routenberg, P. N. Wyrembak, D. B. Turner-Evans, A. D. Hamilton, D. A. LaVan, T. M. Fahmy, and M. A. Reed, *Nature (London)* **445**, 519 (2007).
- <sup>12</sup>P. Bergveld, *Sens. Actuators B* **88**, 1 (2003).
- <sup>13</sup>S. M. Sze, *Physics of Semiconductor Devices*, 2nd ed. (Wiley, New York, 1981), Chap. 5, p. 160.
- <sup>14</sup>X. Wang, Y. Chen, M. K. Hong, S. Erramilli, and P. Mohanty (unpublished).
- <sup>15</sup>P. Nelson, *Biological Physics: Energy, Information, Life*, 1st ed. (W. H. Freeman, New York, 2004), Chap. 5, p. 285.

## Silicon-based nanochannel glucose sensor

Xihua Wang, Yu Chen, Katherine A. Gibney<sup>a)</sup>  
Shyamsunder Erramilli, and Pritiraj Mohanty<sup>b)</sup>

Department of Physics, Boston University, 590 Commonwealth Avenue, Boston, Massachusetts 02215, USA

(Received 15 November 2007; accepted 17 December 2007; published online 8 January 2008)

Silicon nanochannel biological field effect transistors have been developed for glucose detection. The device is nanofabricated from a silicon-on-insulator wafer with a top-down approach and surface functionalized with glucose oxidase. The differential conductance of silicon nanowires, tuned with source-drain bias voltage, is demonstrated to be sensitive to the biocatalyzed oxidation of glucose. The glucose biosensor response is linear in the 0.5–8 mM concentration range with 3–5 min response time. This silicon nanochannel-based glucose biosensor technology offers the possibility of high density, high quality glucose biosensor integration with silicon-based circuitry.

© 2008 American Institute of Physics. [DOI: 10.1063/1.2832648]

Field effect devices, such as capacitive electrolyte-insulator-semiconductor sensor, light-addressable potentiometric sensor, and ion-sensitive field effect transistor (ISFET) for glucose detection,<sup>1–3</sup> have been extensively studied in recent years. Although these devices are limited by the dependence of the sensor response on buffer capacity, ionic strength, and pH of the test sample, their compatibility with advanced microfabrication technology may enable their potential commercialization. Glucose biosensor is a particularly attractive enzyme biosensor due to its potential widespread use in clinical applications.

Currently, glucose detection is mostly limited to *in vitro* test of blood samples, although it is more meaningful to perform *in vivo* test by implantable sensing devices for continued monitoring of blood glucose level. To this end, nanoscale sensors may be fundamentally valuable. Semiconductor nanowires, grown from bottom-up approach, have been demonstrated as good candidates for ultrasensitive biosensors in many applications.<sup>4–6</sup> However, most of the existing studies based on bottom-up approaches face the limitation of complex integration and scalable large-scale manufacturing. Fabrication of silicon nanoscale devices with top-down approaches<sup>7,8</sup> using lithography has the inherent benefit of standard semiconductor processes and, hence, better control of device properties. Therefore, field effect devices, using nanoscale technology, offer the possibility of high-performance, low-cost implantable glucose biosensors.

Here, we demonstrate silicon nanochannels, surface functionalized with glucose oxidase, as a field effect glucose biosensor. The glucose biosensor with a set of silicon nanowires as nanochannels, 50–100 nm wide, 100 nm high, and 6  $\mu\text{m}$  long, is fabricated from a silicon-on-insulator (SOI) wafer. Figure 1 shows a typical scanning electron micrograph of the device. The SOI wafer consists of a 100 nm thick silicon top layer, a 500  $\mu\text{m}$  silicon substrate, and a 380 nm  $\text{SiO}_2$  insulation layer in between. The silicon top layer is lightly doped with boron concentration,  $10^{-15} \text{ cm}^{-3}$ , as the device layer. The silicon nanowires are patterned with electron beam lithography, and two sidewalls are exposed after reactive ion etching. The Ti/Au layer is deposited with

thermal evaporator to function as the source and drain contact electrodes without further annealing. The silicon nanowires are covered with a layer of 10 nm  $\text{Al}_2\text{O}_3$ , grown by atomic layer deposition, to prevent current leakage between analyte solution and silicon nanowires.

Before modification, the  $\text{Al}_2\text{O}_3$  surface is treated with oxygen plasma<sup>9</sup> for two purposes: to clean the sample surfaces and to generate a hydrophilic surface. The wires are first modified by APTES (3% in ethanol with 5% water). Then 3% glucose oxidase in acetic chloride (50 mM) buffer (pH of 5.1) (5% glycerol, 5% BSA) is deposited on the sample and kept in glutaraldehyde vapor for 40 min. The sample is dried in air for 15 min. Glucose samples are made in solution with 50 mM NaCl and 50 mM (or 81.8 mM) of potassium ferricyanide.

All electrical measurements are done at room temperature. The voltage  $V$  across the nanowires is applied by using a modulated sine wave source upon dc bias. The current  $I$  across the nanowires is converted into voltage by a feedback resistor, and this voltage is detected with a lock-in amplifier. A voltage is applied on the Ag/AgCl reference electrode contacted with solution as the reference gate voltage,  $V_{\text{rg}}$  (Ref. 7). This allows direct, real-time measurement of the differential conductance  $g = (\partial I / \partial V)_{V_{\text{rg}}}$ . In particular, the method allows studies at zero bias and reverse bias as well.

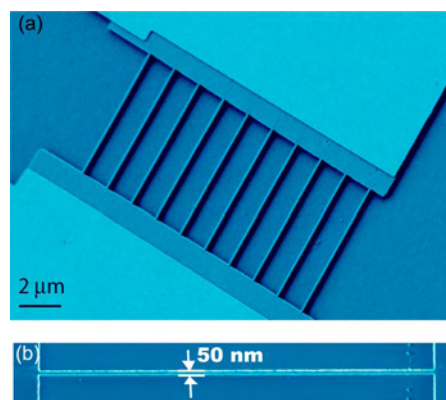


FIG. 1. (Color online) (a) Scanning electron micrograph of silicon nanowires, the working part of the biosensor. (b) Top view of a 50 nm wide nanowire shows the controlled linear geometry.

<sup>a)</sup>Present address: Department of Chemistry, University of Michigan, 930 N. University, Ann Arbor, MI 48109-1055, USA.

<sup>b)</sup>Electronic mail: mohanty@physics.bu.edu.



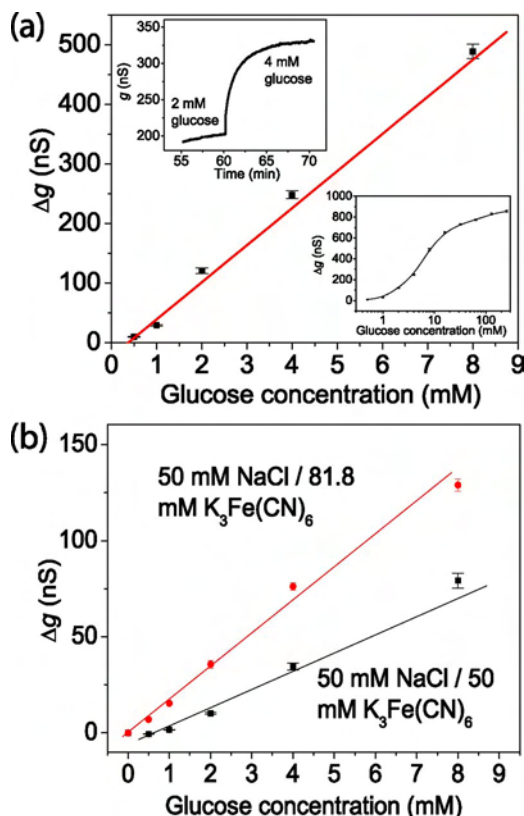
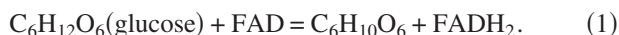


FIG. 2. (Color online) (a) The glucose biosensor response in the 0.5–8 mM concentration range, which is fitted into a linear curve.  $V_{ds} = -0.69$  V,  $V_{rg} = 0$  V. All solutions contain 50 mM of NaCl and 50 mM of potassium ferricyanide. The top inset shows the real time differential conductance change due to exchange glucose solutions. The bottom inset is differential conductance of the device versus glucose concentration. The random error is estimated to be 5% of the device response due to the addition of different glucose solutions. (b) Device responses for 81.8 mM (red curve) and 50 mM (black curve) potassium ferricyanide solutions are displayed.

Figure 2(a) gives the real-time device response when we add glucose solutions upon initial use. We find that there is a linear relation between device response and glucose concentration in the range of 0.5–8 mM. From the response curve [the bottom inset of Fig. 2(a)], we find that the differential conductance change of the device reaches saturation after the glucose concentration of 16 mM. We can also estimate the diffusion-limited time response of the device to be 3–5 min, which is the same as the typical response times of thick-layer glucose oxidase modified ISFET.<sup>10</sup> The response time could be further improved by enzyme monolayer functionalization.<sup>11</sup>

The oxidation of glucose catalyzed by glucose oxidase is a two-substrate reaction.<sup>12</sup> One molecule of glucose oxidase contains two molecules of oxidized form of flavine adenine dinucleotide (FAD). In the first substrate reaction, there is a formation of an enzyme-glucose complex, and then the FAD is reduced according to



The reduced form of the enzyme is fast oxidized by oxygen, producing hydrogen peroxide, and it restores the initial state of the enzyme molecule



In the second substrate reaction, the generated gluconolactone ( $C_6H_{10}O_6$ ) is hydrolyzed spontaneously to gluconic acid

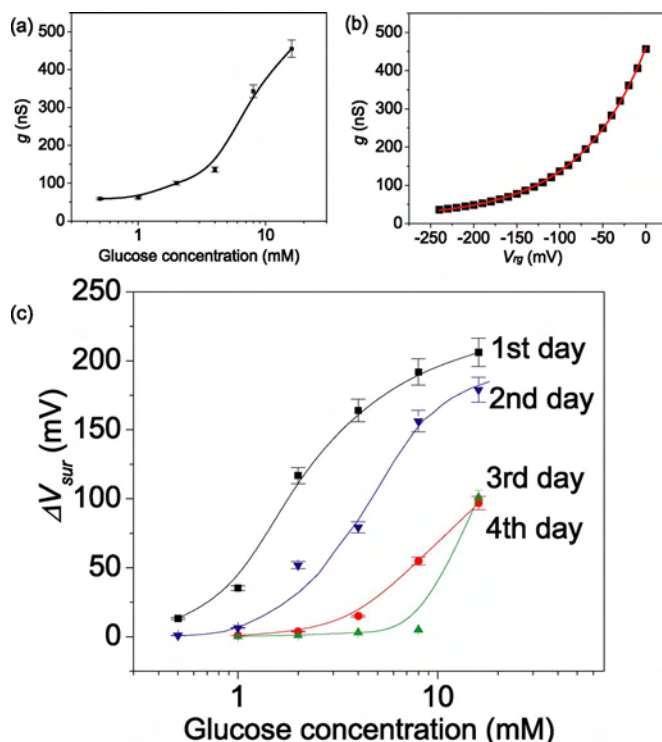
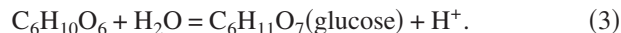


FIG. 3. (Color online) (a) Device response as a function of glucose concentration, taken on the second day. (b) Device response as a function of the reference gate voltage in 16 mM glucose solution, taken on the second day. (c) Calibrated surface potential change vs. glucose concentration, taken on different days. All solutions contain 50 mM of NaCl and 81.8 mM of potassium ferricyanide.



Therefore, one glucose molecule yields one hydrogen ion, and it changes the local hydrogen ion activity of the solution. In our earlier work, we have shown that the top-down fabricated sensors are sensitive to pH, which quantifies the hydrogen ion concentration. Changes in the local hydrogen ion concentration alter the surface potential and, hence, the electric field which modulates the conductance of the BioFET. This field effect is further amplified by adding ferricyanide ions  $\{[\text{Fe}(\text{CN})_6]^{3-}\}$ :

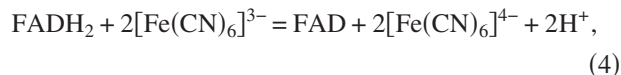


Fig. 2(b) confirms this effect. An 81.8 mM potassium ferricyanide solution has the sensitivity of 16 nS/mM, while a 50 mM potassium ferricyanide solution gives the sensitivity of 10 nS/mM. So higher concentration of potassium ferricyanide yields higher sensitivity.

To evaluate the device performance and degradation as the function of calibrated surface potential, similar to the macroscopically large ISFET experiments,<sup>13</sup> we have measured the calibrated plot of surface potential change. The surface potential  $V_{sur}$  is offset from the reference electrode potential because of contact potential drop and electrolytic screening effects. However, the change in surface potential  $\Delta V_{sur}$  induced by oxidation reaction is equal to the change in reference electrode voltage  $\Delta V_{rg}$  applied to achieve the same device response in the solution. This is consistent with our previous experiments, in which we showed the equivalence between changing reference electrode voltage and changing analyte concentration in solution.<sup>14</sup> Figure 3 shows a plot of

the calibrated surface potential change versus glucose concentration. First, we perform real-time differential conductance measurements by changing glucose concentration [Fig. 3(a)]. Then, at the same  $V$  in the 16 mM glucose solution, we perform a rapid scan of  $V_{rg}$  to obtain a similar plot [Fig. 3(b)]. The differential conductance of the device is fitted with an exponential growth function of the reference gate voltage,

$$\left(\frac{dI}{dV}\right)_{V_{rg}} = G_0 + G_1 \exp\left(\frac{V_{rg}}{V_\tau}\right), \quad (5)$$

and the value of  $V_\tau$  is found to be 77 mV for the listed sample. This fitting parameter implies how the device conductance changes according to surface potential change by adding analyte concentration. Lower value of  $V_\tau$  gives higher sensitivity of the device. Using the data from these two measurements, we can plot the calibrated surface potential change versus glucose concentration by converting device response into an equivalent surface potential change. In this step, we convert each differential conductance of the device in different solutions into an equivalent reference gate voltage by using the curve in Fig. 3(b), and we count the voltage difference between different solutions. The final plot of calibrated surface potential change as the function of glucose concentration is shown as the second day curve in Fig. 3(c). From the first day curve, the slope of 160 mV/decade change of glucose concentration is observed. The slope decreases after operation of several days, implying degradation of device performance. This degradation is attributed to a side reaction of the released hydrogen peroxide, which can directly oxidize and deactivate of the enzyme on the device surface. Thus, the application of the device is limited to short-term use. However, long-term use could be achieved by inducing a secondary active electrode near nanowires to eliminate degradation.<sup>12</sup>

Taken together, our studies show that the nanowire sensors provide an excellent platform for disposable glucose sensors. In order to implement the sensors for long-term implantable use, a solution to the degradation problem is needed. One suggestion first proposed for macroscale ISFET

using a control electrode to counteract the effect of the peroxide appears to be promising. It would be important to extend the performance of nanowire sensors by exploiting a similar idea.

In conclusion, we have fabricated silicon nanowires as glucose biosensor. In the differential conductance measurement, the device response has a linear range for glucose concentration between 0.5 and 8 mM upon initial use. While the calibrated surface potential versus glucose concentration plot gives the maximum slope of 160 mV/decade. The device also performs with a reasonable response time of 3–5 min. The linear glucose detection range, fast response time, and detection limit provide a pathway to fabricate high-density, high-performance nanoscale glucose biosensors that can be integrated with silicon-based circuitry.

The authors acknowledge support by the Department of Defense and the National Science Foundation.

- <sup>1</sup>A. Seki, S. Ikeda, I. Kubo, and I. Karubo, *Anal. Chim. Acta* **373**, 9 (1998).
- <sup>2</sup>M. J. Schöning and A. Poghosian, *Electroanalysis* **18**, 1893 (2006).
- <sup>3</sup>S. V. Dzyadevich, Y. I. Korpan, V. M. Arkhipova, M. Yu. Alesina, C. Martelet, A. V. EL'skaya, and A. P. Soldatkin, *Biosens. Bioelectron.* **14**, 283 (1999).
- <sup>4</sup>Y. Cui, Q. Wei, H. Park, and C. M. Lieber, *Science* **293**, 1289 (2001).
- <sup>5</sup>G. Zheng, F. Patolsky, Y. Cui, W. U. Wang, and C. M. Lieber, *Nat. Biotechnol.* **23**, 1294 (2005).
- <sup>6</sup>K. Besteman, J.-O. Lee, F. G. M. Wiertz, H. A. Heering, and C. Dekker, *Nano Lett.* **3**, 727 (2003).
- <sup>7</sup>Y. Chen, X. Wang, S. Erramilli, P. Mohanty, and A. Kalinowski, *Appl. Phys. Lett.* **89**, 223512 (2006).
- <sup>8</sup>E. Stern, J. F. Klemic, D. A. Routenberg, P. N. Wyrembak, D. B. Turner-Evans, A. D. Hamilton, D. A. LaVan, T. M. Fahmy, and M. A. Reed, *Nature (London)* **445**, 519 (2007).
- <sup>9</sup>Z. Li, Y. Chen, X. Li, T. I. Kamins, K. Nauka, and R. S. Williams, *Nano Lett.* **4**, 245 (2004).
- <sup>10</sup>B. K. Sohn, B.-W. Cho, C.-S. Kim, and D.-H. Kwon, *Sens. Actuators B* **41**, 7 (1997).
- <sup>11</sup>A. B. kharitonov, M. Zayats, A. Lichtenstein, E. Katz, and I. Willner, *Sens. Actuators B* **70**, 222 (2000).
- <sup>12</sup>A. A. Shul'ga, M. Koudeika-Hep, and N. F. de Rooij, *Anal. Chem.* **66**, 205 (1994).
- <sup>13</sup>P. Bergveld, *Sens. Actuators B* **88**, 1 (2003).
- <sup>14</sup>Y. Chen, X. Wang, M. K. Hong, S. Erramilli, P. Mohanty, and C. Rosenberg, *Appl. Phys. Lett.* **91**, 243511 (2007).